Geoejector: Extracting geothermal fluid from a low-pressure geothermal well

Jeffrey Macatangay Andal

Thesis of 60 ECTS credits
**Master of Science (M.Sc.) in Sustainable Energy
Engineering**

June 2023

Geoejector: Extracting geothermal fluid from a low-pressure geothermal well

Thesis of 60 ECTS credits submitted to the School of Science and Engineering
at Reykjavík University in partial fulfillment of
the requirements for the degree of
**Master of Science (M.Sc.) in Sustainable Energy
Engineering**

June 2023

Supervisors:

María Sigríður Guðjónsdóttir, Ph. D.
Associate Professor, Reykjavík University, Iceland

Guðrún Arnbjörg Sævarsdóttir, Ph. D.
Professor, Reykjavík University, Iceland

Egill Júlíusson, Ph. D.
Chief Technology Officer, Arctic Green Energy Corporation

Examiner:

Ásdís Helgadóttir, Ph. D.
Associate Professor, University of Iceland, Iceland

Geoejector: Extracting geothermal fluid from a low-pressure geothermal well

Jeffrey Macatangay Andal

June 2023

Abstract

To utilize a low-pressure and low-enthalpy well, a subsonic ejector system (referred to as subsonic geoejector) was developed and tested at the Theistareykir Geothermal Field in 2020 and 2021. The system connected a low-pressure geothermal well to a nearby high-pressure well to induce flow from the low-pressure well under otherwise unfavorable pressure. The subsonic geoejector has similar working principle as an industrial ejector used in many industries. However, unlike traditional ejectors, it is faced with challenges involving two-phase geothermal fluids and highly variable inflow conditions. From analysis with an analytical and numerical model of the subsonic geoejector, it was found that it cannot accelerate the high-pressure fluid enough to create an underpressure that will induce flow from the low-pressure well under real operating conditions. To address this problem, this paper will introduce a supersonic geoejector that was designed to meet the operational requirement for power production and analyzed with an analytical and numerical model. The result of the models are promising, and it is found that the new setup could potentially increase the pressure of geothermal fluid from low-pressure well sufficiently or up to 2.4 bar, which would add up to 0.8 MWe for power generation.

Geoejector: Að draga jarðhitavökva úr lágþrýsti jarðhitaholu

Jeffrey Macatangay Andal

júní 2023

Útdráttur

Til að nýta lágþrýsta og lágvermis gufuborholu var settur upp jektor með vökvahraða undir hljóðhraða (kallaður subsonic geoejector) og hann prófaður á Þeistareykjum á árunum 2020 og 2021. Kerfið tengdi lágþrýsta jarðhitaholu við nærliggjandi háþrýstiholu til að framkalla flæði úr lágþrýstiholunni við annars óhagstæðan bakþrýsting. Jektorinn er sambærilegur við jektora sem notaðir eru í ýmsum atvinnugreinum. Ólíkt hefðbundnum jektorum, er mikil áskorun fólgin í því að tveggja fasa jarðhitavökvi streymir um hann og innstreymið er mjög breytilegt. Út frá greiningu með analýtísku og tölulegu líkani af jektornum með vökvarennsli undir hljóðhraða kom í ljós að hann getur ekki hraðað háþrýstivökvanum nógu mikið til að búa til undirþrýsting til þess að viðhalda flæði frá lágþrýstiholunni við raunverulegar rekstraraðstæður. Til að bregðast við þessu vandamáli mun þessi grein kynna jektor með vökvarennsli yfir hljóðhraða (e. supersonic geoejector), sem var hannaður til að uppfylla rekstrarþörf fyrir orkuframleiðslu og greindur með analýtísku og tölulegu líkani. Niðurstaða líkansins lofar góðu og bendir til að nýja uppsetningin gæti aukið þrýsting jarðhitavökva úr lágþrýstiholu um 2,4 bör, sem myndi bæta við allt að 0,8 MW_e í raforkuframleiðslu.

Geoejector: Extracting geothermal fluid from a low-pressure geothermal well

Jeffrey Macatangay Andal

Thesis of 60 ECTS credits submitted to the School of Science and Engineering
at Reykjavík University in partial fulfillment of
the requirements for the degree of
Master of Science (M.Sc.) in Sustainable Energy Engineering

June 2023

Student:

_____
Jeffrey Macatangay Andal

Supervisors:

_____
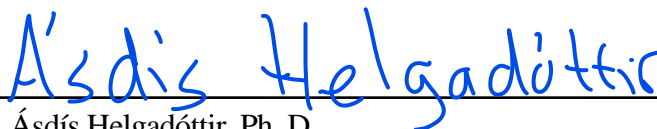María Sigríður Guðjónsdóttir, Ph. D.

_____
Guðrún Arnbjörg Sævarsdóttir, Ph. D.

_____
Egill Júlíusson, Ph. D.

Examiner:

_____
Ásdís Helgadóttir, Ph. D.

x

The undersigned hereby grants permission to the Reykjavík University Library to reproduce single copies of this Thesis entitled **Geoejector: Extracting geothermal fluid from a low-pressure geothermal well** and to lend or sell such copies for private, scholarly or scientific research purposes only.

The author reserves all other publication and other rights in association with the copyright in the Thesis, and except as herein before provided, neither the Thesis nor any substantial portion thereof may be printed or otherwise reproduced in any material form whatsoever without the author's prior written permission.

June 06, 2023
date

Jeffrey Macatangay Andal
Master of Science

I dedicate this to my family and to the geothermal energy stakeholders.

Acknowledgements

Preface

This dissertation is original work by the author, Jeffrey Macatangay Andal. Portions of these dissertation are used with permission from the submitted papers by the geoejector research team for the World Geothermal Congress 2023 in Beijing, China, of which I am one of the authors.

Contents

List of Figures

List of Tables

List of Abbreviations

AM	Analytical model
CFD	Computational Fluid Dynamics
ER	Entrainment ratio
FT	Field test
IAPWS	International Association for the Properties of Water and Steam
MW_e	Megawatt electric
MW_t	Megawatt thermal
NM	Numerical model
NXP	Primary nozzle position

List of Symbols

Symbol	Description	Value/Units
a	Sonic velocity	m/s
A	Area	m^2
c_l	Coefficient of frictional and mixing losses	
C_p	Specific Heat in constant pressure	kJ/kg-°C
C_v	Specific Heat in constant pressure	kJ/kg-°C
D	Diameter	cm
E	Total exergy	kJ
e	Total specific energy	kJ/kg
$\dot{e}$	Specific exergy rate of component	kJ/kg
$\dot{E}$	Exergy rate	kW
ER	Entrainment ratio	
h	Enthalpy	kJ/kg
$\dot{H}$	Enthalpy flow rate	kW
k	Ratio of specific heats	
L	Length	cm
$\dot{m}$	Mass flow rate	kg/s
M	Mach number	
NXP	Primary nozzle position	cm
p	Pressure	Bar-g
s	Entropy	kJ/kg-K
T	Temperature	°C
v	Fluid velocity	m/s
x	Steam quality	
α	experimental constant	
ϵ_k	Exergetic efficiency	%
$\Delta\dot{H}_u$	Change in useful energy	kW
η_{energy}	Energy efficiency	%
$\eta_{\Delta\dot{H}_u}$	Energy conversion efficiency	%
η_n	Isentropic efficiency	%
ρ	Density	kg/m^3

Symbol	Description	Value/Units
Subscripts and superscripts for subsonic geoejector		
0	Stagnation point	
1	Primary flow inlet	
2	Nozzle exit	
3	Primary flow at mixing section	
4	Secondary flow inlet	
5	Suction line or secondary at mixing section	
6	Mixed flow at mixing section	
7	Throat	
8	Diffuser exit or geoejector outlet	
*	Critical values at sonic point	
Subscripts and superscripts for supersonic geoejector		
CAMS	Stagnation point	
0	Primary flow inlet	
1	Nozzle throat	
2	Nozzle exit	
3	Point between the nozzle exit and hypothetical throat	
3.5	Primary flow at the hypothetical throat	
4	Secondary flow inlet	
5	Entrained flow at the hypothetical throat	
6	Entrained flow at the hypothetical throat	
7	Hypothetical throat or cross-sectional area inside the constant area mixing section	
8	Shockwave within the constant area mixing section	
9	Diffuser exit / Ejector outlet	
*	Critical values at sonic point	
Subscripts and superscripts for energy and exergy analysis		
0	Environmental or dead state	
CH	Chemical	
d	Destruction	
f	Fuel	
g	Saturated vapor	
k	Component	
KN	Kinetic	
l	Losses	
p	Product	
PH	Physical	
PO	Potential	

Chapter 1

Introduction

Drilling geothermal wells is one of the primary costs drivers to any geothermal project, ranging from 32 to 37% of a project's total investment (Gehringer, M. and Loksha, V.C., 2012). Aside from the cost, the drilling also involves high risk with success rates of wells ranging from 59 to 83% depending on the project phase (IFC, 2013). One of the reasons a well is regarded unsuccessful is when the pressure of the fluid from the well is below the threshold to be connected to the steam gathering system of the associated plant. To address this problem at the Theistareykir Geothermal Field, a rudimentary ejector system, referred to in this study as a subsonic geoejector, was built and tested in 2020 and 2021. These tests aimed to connect to a nearby high-pressure geothermal well, THG-11, to induce flow from a low pressure and enthalpy geothermal well, THG-15, by creating a localized underpressure where the two streams meet.

An ejector is a static device that converts the pressure of a high-pressure primary stream into kinetic energy to draw or entrain a fluid from a low-pressure secondary source. The two streams will then mix and discharge into a diffuser to convert the kinetic energy back into increased pressure. Ejectors are relatively common and have a variety of applicability in different industries such as refrigeration, power generation, and chemical sectors. Additionally, this technology has a minimal maintenance requirement due to their nonmoving parts, low operating expenses, and limited constraints on the working fluid (Besagni, G., 2019).

Limited information can be found regarding the application of ejectors to recover geothermal fluids from low-pressure wells. In 1999, an ejector apparatus to increase the fluid recovery from geothermal wells was patented (Jung, D. B., 1999). However, according to Gutsol, A. F. (Gutsol, A. F., 2018), the ejector field test did not validate the patent's claim and it was likely caused by the problem on the ejector parameters. Unfortunately, no calculation method for the ejector parameters was disclosed in the patent.

In the current work, the ejector used for this purpose is referred as a geoejector. To analyze the performance of a geoejector, this study looked into several studies in different industries that investigated the effect of geometrical parameters on ejector performance were reviewed. Keenan and Neuman proposed a 1-D constant pressure mixing ejector theory to analyze the performance of an ejector (Keenan, J. H. & Neuman, E. P., 1942). This model was later improved by considering the thermodynamic irreversibility and real gas behavior (Keenan, J. H. & Neuman, E. P., 1950). Another study proposed that after the primary flow is discharged from the ejector's nozzle exit, it fans out without mixing with the entrained flow and induces the latter to a converging duct within the mixing chamber. This converging duct accelerates the entrained flow to a sonic velocity at some point inside the converging duct known as the "effective area" or the "hypothetical throat". Downstream of the hypothetical throat the mixing of the two streams occurs with a uniform pressure (Munday, J. T. & Bagster, D. F., 1977). Huang et al. assumed that the hypothetical throat occurs inside the constant area

mixing section of the ejector and built a 1-D model to predict performance while the ejector is in critical mode or double choking (Huang et al., 1999). One of the challenges of the 1-D model for ejectors was determining the speed of sound in a two-phase flow. To circumvent this problem, the mass flux maximization criterion was introduced by Ameur et. al (Ameur, et al., 2016). Chen et al. developed a theoretical model that analyses ejector performance under critical and sub-critical modes (Chen et al., 2017). The model from Chen et al. compared reasonably to experimental and theoretical results from the literature (Huang et al., 1999, Aphornratana et al., 2001).

The continuous development of theoretical or analytical models provides remarkable achievement in predicting the performance of an ejector. The analytical models however, was unable to accurately duplicate the flow regime within the ejector. One way to obtain such information is by using computational fluid dynamics (CFD) (Bartosiewicz et al., 2005). CFD is an established analysis and design tool that is used as a cost-effective and accurate alternative to scale model testing (ANSYS Inc., 2023a).

The flow regime inside an ejector is complicated, making CFD or numerical modeling complex. According to studies, the relative error between the numerical model and the experimental data could range from 20 to 100% (Ringstad et al., 2020). Notwithstanding significant discrepancies with the experimental data, studies revealed that the numerical model could achieve a good agreement with the pressure profile inside an ejector (Sriveerakul et al., 2007, Colarossi et al., 2012). Furthermore, the numerical modeling is crucial because it can provide information on the underlying transport mechanisms for heat, momentum, and mass transfer that an analytical model cannot.

The field tests at Theistareykir employed a rudimentary subsonic geoejector. The high-pressure geothermal well was operated below its nominal operating capacity due to the limitation of the separator used during the tests. Using analytical and numerical modelling, the flow regime inside the subsonic geoejector will be predicted to determine the factors that influence its performance and its applicability to operate the high-pressure geothermal well to its normal operating condition. Further, the information obtained from these models was then used in the analytical model of the supersonic geoejector to determine the geometric parameters and to predict its performance under realistic operating conditions. The analytical model used for the supersonic geoejector was largely based on the models developed by Huang et al. (Huang et al., 1999) and Chen et al. (Chen et al., 2017). To analyze the performance of the supersonic geoejector, experimentation is the most reliable approach. However, due to the time and resource costs it requires to design the experiment, numerical modelling was employed to determine the underlying transport phenomena for heat, momentum, and mass transfer.

The use of a geoejector has the potential to increase the power generation by extracting energy from idle or non-operational wells. The existence of both high- and low-pressure well within the geothermal field is not unique to Theistareykir; similar case can be seen in several geothermal fields in the Philippines (DOE, 2023) and is believed to be present in other high-temperature steamfields around the world. This work is considered a first step in developing a practical and economical geoejector that employs the flow of a high-pressure well to induce flow from a well at lower pressure, thus connecting it to the steam gathering system. The model does not yet address major challenges expected under real operations, such as scaling, presence of liquid water in the secondary flow, and highly transient inflow.

Chapter 2

Field test at Theistareykir Geothermal Production Field

This chapter describes the wells and setup used during the field test at Theistareykir Geothermal Field in 2020 and 2021. This chapter also discusses the performance indicators that would be used to assess the success of using a geoejector to extract geothermal fluid from a low-pressure and low-enthalpy well.

2.1 Wells THG-11 and THG-15

The subsonic geoejector used in the field test at Theistareykir Geothermal Field connected wells THG-11 and THG-15 as the high-pressure fluid source (primary) and the low-pressure fluid source (secondary), respectively.

Well THG-11 is a production well that was drilled in July 2016 and is a high-pressure well, which has a well head potential of 14.4 MWe. Well THG-15, located on the same well pad as THG-11, was drilled in March 2017 and is a low-pressure well, which is below the threshold to be connected at the steam gathering system (Mkangala, A., 2017, Egilson, T., 2019). Further information about the wells is shown in Table 2.1.

Table 2.1 Properties of wells THG-11 and THG-15 (Egilson, T., 2019).

Well name	Depth (m)	Measured mass flow rate at reported wellhead pressure(kg/s)	Reported well head pressure (bar-g)	Enthalpy (kJ/kg)	Well head potential (MWe)[1]	Status[1]
THG-11	2224	26	30	2700	14.4	In use
THG-15	2260	14	8.7	950	2.0	Not in use

[1] (Knútsson, et al., 2018).

The wellhead pressure of THG-11 is currently reduced to the steam gathering system pressure (9.5 – 10 bar-g) through orifice plates. On the other hand, the wellhead pressure of THG-15 is not high enough to reliably enter the system (i.e. minor fluctuations in the line pressure cause the well to choke) and has therefore not been in use.

From the recent well measurement data and recommendations from the power plant operators, the pressure from THG-11 considered in this paper ranges from 10 to 25 bar-g. Additionally, the well was determined to have a maximum mass flow rate of 30 kg/s. Well THG-15 has a maximum wellhead pressure of 9 bar-g. However, there is no recent well measurement to determine its maximum mass flow rate. Furthermore, it was recommended that the liquid coming from the stream of THG-15 should be mixed to the stream coming from

THG-11, as it was believed to be a solution to the latter's silica scaling problem by functioning as a wet scrubbing medium.

2.2 Field test setup

During the field test setup, as shown in Figure 2.1, THG-11 and THG-15 were connected to the primary and secondary inlet of the geoejector, respectively, and the outlet was connected to a separator. It should be noted that the separator used was inadequately large to support the entire capacity of THG-11 and THG-15; with this in consideration, THG-11 operated at a higher well head pressure to reduce mass flow. After that, the pressure was reduced using pressure control valve and orifice plates before entering the geoejector.

(a)   (b)
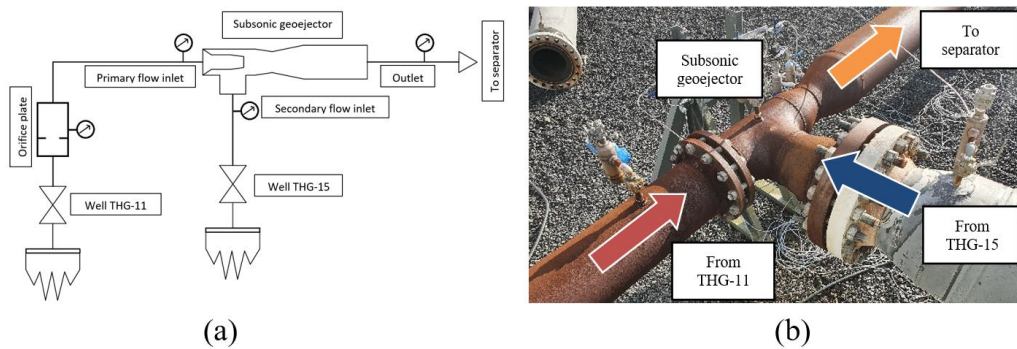
Figure 2.1 (a) Schematic diagram of the field test setup and (b) picture of the geoejector during field test.

2.3 Measurements and data collection

Landsvirkjun conducted field testing at Theistareykir Geothermal Field in 2020 and 2021. As a result, the field test analysis will be based on the gathered data and operator's log sheet provided by Landsvirkjun.

The data provided consists of several measurements taken at various points within the subsonic geoejector setup, see Figure 2.1. To analyze the performance of the subsonic geoejector, the pressure and enthalpy in both inlets, differential pressure in the orifice plate near THG-11, and total mass flow and enthalpy at the outlet were used among the available data. The mass flow rate at the primary inlet was estimated using the differential pressure at the orifice plate and was validated in the operator's log sheet's set-in mass flow. The mass flow rate at the secondary inlet, or the entrained flow, was calculated by subtracting the mass flow rate at the primary inlet to the total mass flow rate at the outlet. Nevertheless, some of the test results were not satisfactory (i.e. missing measurement data and mass flow readings could not be validated) to make a comprehensive analysis of the subsonic geoejector's performance. Still, several field measurements from September 1 to 8, 2021, were available for study. Figure 2.2 shows an overview of the collected data. It should be noted in the figure that there was a break period between September 2 and September 8.
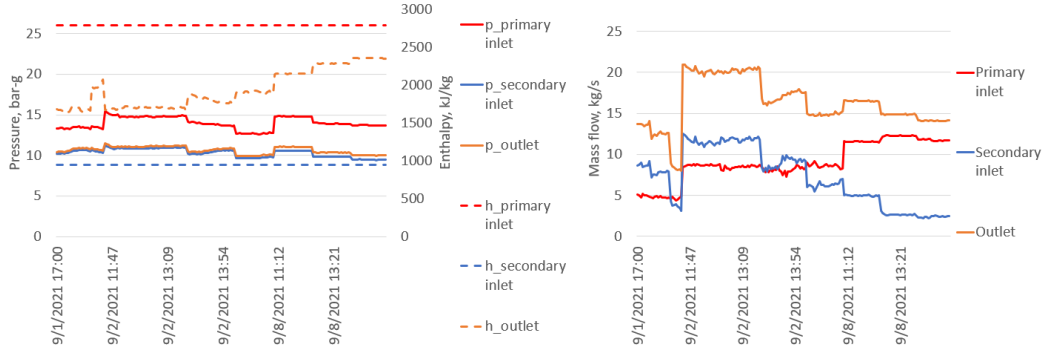
Figure 2.2 Overview of the field test data conducted from September 01 to 08, 2021.

According to the Operator's log sheet, the field test from September 1 to 2 and September 8 follow different procedures.

The following procedures were followed for September 1 to 2:
1. Set mass flow from the primary well.
2. The inlet for the secondary well was then fully opened.
3. the separator valve tightened to set the back pressure in the system.

The following procedures were followed for September 8:
1. Set mass flow from the primary well.
2. The inlet for the secondary well was then fully opened.
3. The valve in the secondary inlet was occasionally tightened.

2.4 Performance indicators

For this study, three performance indicators were used to assess the success of using the subsonic geoejector to extract geothermal fluids from low-pressure and enthalpy well. The following performance indicators are used:
1. Entrainment ratio (ER): the ratio of the mass flow rate between secondary and primary flow (see Equation 2.1).
2. Induced pressure: the difference between the outlet's pressure and secondary flow inlet's pressure (see Equation 2.2).
3. Change in useful energy ($\Delta \dot{H}_u$): the difference between the energy from the outlet's separated steam and the energy from the primary flow's steam input (see Equation 2.3). For this performance indicator, it was assumed that the mixed fluid exiting the geoejector was separated in its gas and liquid phase at constant pressure at the outlet. The energy from the secondary flow's steam input was not considered because the THG-15 could not connect directly to the system due to its vulnerability to pressure fluctuations.

$$ER = \frac{\dot{m}_{secondary}}{\dot{m}_{primary}}$$

(2.1)

$$Induced\ pressure\ =\ p_{outlet} - p_{secondary}$$

(2.2)

$$\Delta \dot{H}_u\ =\ \dot{m}_{g(outlet)} h_{g(outlet)} - \dot{m}_{primary} h_{primary}$$

(2.3)

Chapter 3

Analytical model for geoejector

The flow regime inside the geoejector, like a normal ejector, is complex as it involves subsonic, transonic and supersonic fluid flows, interaction between the primary and secondary flows with large velocity gradient, shock waves, and two-phase fluid flow (Šarevski, V. V. & Šarevski, M., 2019). Simplifications and assumptions within the flow regime inside the geoejector are necessary to establish a basis in developing the analytical model for the geoejector.

The two types of geoejectors examined in this study are the subsonic and supersonic geoejector. The rudimentary geoejector employed during the field test at Theistareykir Geothermal Field is the subsonic geoejector. The supersonic geoejector, on the other hand, is the improved design considered to address the problems found using the subsonic geoejector. The main difference between these two geoejectors is the nozzle; the subsonic geoejector has a converging nozzle, while the supersonic geoejector has a converging-diverging nozzle. Additionally, the supersonic geoejector has a narrower and longer mixing section's throat, also known as a constant area mixing section, than the subsonic geoejector.

This chapter will provide the simplifications and assumptions that were used in the development of the analytical model for the geoejectors. This chapter will also go through the energy and exergy analysis, which will be used to illustrate the energy and exergy flow inside the system.

3.1 Subsonic geoejector

Theistareykir Geothermal Field's rudimentary subsonic geoejector, as shown in Figure 3.1, varies from conventional subsonic ejectors used in other industries by having a short throat. The absence of a longer throat is predicted to have a direct impact on the geoejector's outlet pressure. Sufficient mixing is required for the momentum transfer between the primary and secondary stream to be completed. This efficient mixing between the two streams can directly affect the regained pressure (Pianthong et al., 2007).
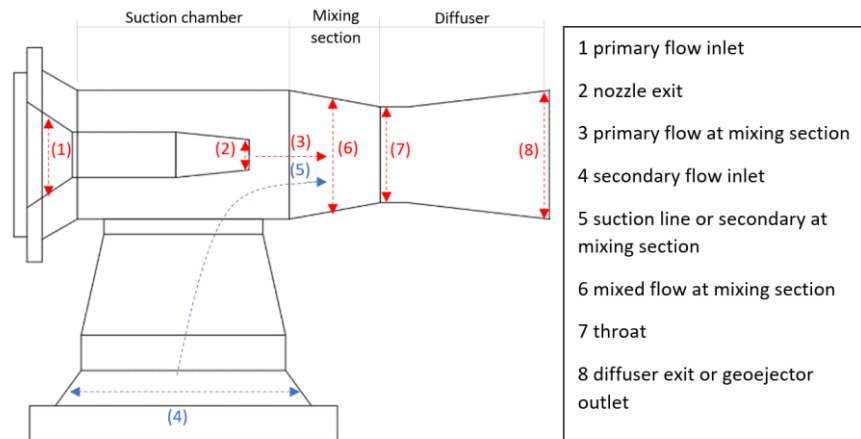
Figure 3.1 Subsonic geoejector used during field test at Theistareykir Geothermal Field.

3.1.1 Flow regime inside the subsonic geoejector

The primary fluid is accelerated through the nozzle (from 1 to 2, each number is represented by the location in Figure 3.1). This acceleration decreases the pressure of the primary fluid allowing the secondary flow to be entrained. It is then assumed that the properties of the entrained flow (5) and the flow coming from the secondary inlet (4) remains unchanged until mixing occurs. The primary flow leaving the nozzle (2) is then assumed to spread without mixing with the entrained flow (3). With the absence of the minimum throat length for an efficient mixing, the flow regime in this rudimentary subsonic geoejector was simplified by assuming that the two streams mixed homogeneously inside the mixing section before entering the throat (6) at constant pressure. The mixed fluid will then pass through the throat (7), which accelerates the mixed fluid. The flow is then decelerated in a diffuser (8) to reach a desired back pressure.

3.1.2 Analytical model for the subsonic geoejector

To understand the data gathered during the field test and to determine the viability of using the technology in full-scale operation, an analytical model for the subsonic geoejector was developed following the flow regime described in Chapter 3.1.1. The model was used to predict the output pressure and enthalpy for given primary and secondary inlet conditions. Further, to develop the model, it requires assumptions and simplifications that are necessary to understand the complex flow in the system. The simplifications and assumptions used in this model were as follows:

1. The model uses a constant specific heat ratio, k, of 1.327 and is based on analytic equations for an ideal gas, even though the fluid is not an ideal gas, to maintain momentum balance. It is important to note that k decreases slowly with increase in temperature. The value used fits well for a temperature range within the geoejector. Therefore, constant specific heat is assumed for the analysis (White, F., 2011).
2. The model treats the two-phase flow from well THG-15 as a homogeneous mixture behaving as an ideal gas (i.e. it uses weighted density and enthalpy, and common pressure and temperature). This is a significant simplification given the low quality of the steam, which raises the importance of phase separation and uncertainty regarding

    the flow regime. However, at this stage, it is a necessary simplification to get an initial geoejector design.

3. Isentropic relations were used to simplify the analytical model derivation. However, to account for non-ideal processes (i.e. effects of frictional and mixing losses), a coefficient of frictional and mixing losses, c_l, and isentropic efficiency, η_n, were used.

    a. The c_l accounted in this model was 0.84. This value was taken from Huang et al. (Huang et al., 1999) wherein it was based on the area ratio between the constant area mixing section and nozzle's throat. In the case of the subsonic geoejector, it had a converging nozzle and no constant area mixing section: therefore, the area ratio was based on the ratio between the throat (7) and the nozzle exit (2). Based on how this coefficient was applied in the analytical model, it was observed that it is similar to efficiency, and so 0.84 reflects the losses within the system is 16%.

    b. The η_n within the geoejector was assumed to be 90%.

4. The primary and secondary flows mix in the mixing chamber before reaching the throat (7). The mixing is assumed to occur at a uniform pressure which is equal to the pressure of the entrained flow (5).

5. The kinetic energies at the primary inlet (1), secondary inlet (4), and diffuser outlet (8) are negligible.

6. The inner walls of the subsonic geoejector are adiabatic, with no heat loss.

7. Effects of the liquid-vapor phase change (i.e. condensation and boiling) are not accounted for in the model.

    Following the processes, simplifications and assumptions used the analytical model developed to assess the performance of the subsonic geoejector used at Theistareykir Geothermal Field is shown on Figure 3.2. The thermophysical properties of the fluid were obtained using CoolProp (Bell, I. H., Wronski, J., Quoilin, S., & Lemort, V., 2014) wherein the equation of state of ordinary water/steam was largely based on IAPWS 95 formulation (Wagner, W. & Pruss, A., 2002).
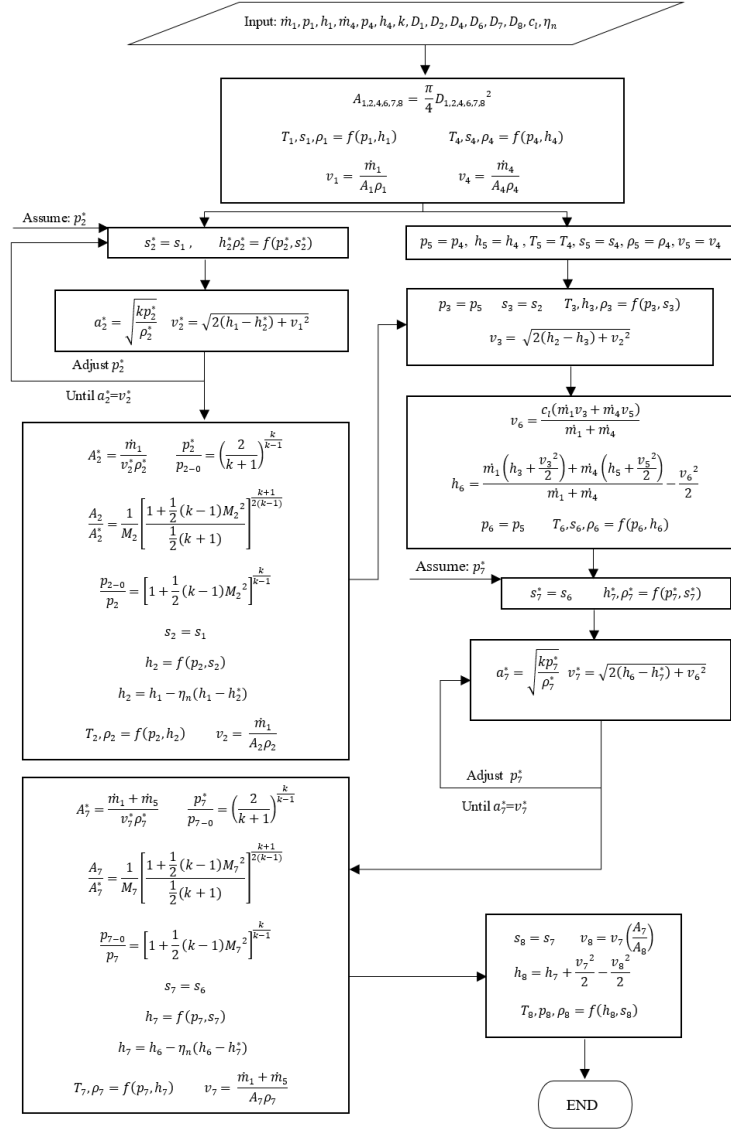
Figure 3.2 Flowchart of the analytical model of the subsonic geoejector.

The geometrical measurements inside the subsonic geoejector or the geometric parameters are fixed and known in this flowchart, as shown in Figure 3.2. Inlet mass flow, pressure, and enthalpy are required from the primary and secondary flow as an input in the model. Following the computations in the flowchart while satisfying the iteration requirements yields the output (pressure and enthalpy at the outlet). Appendix A contains details on the governing equations of the analytical model's processes.

3.2 Supersonic geoejector

The supersonic geoejector was designed to enable improved geoejector performance under the THG-11's normal operating conditions. As shown in Figure 3.3, the supersonic geoejector has a converging-diverging nozzle and a constant area mixing section, as compared to the subsonic geoejector. The various components found in other industries' ejectors are the same as those found in the supersonic geoejector. Meanwhile, the supersonic geoejector's geometric parameters were modified based on the calculations described in this chapter.
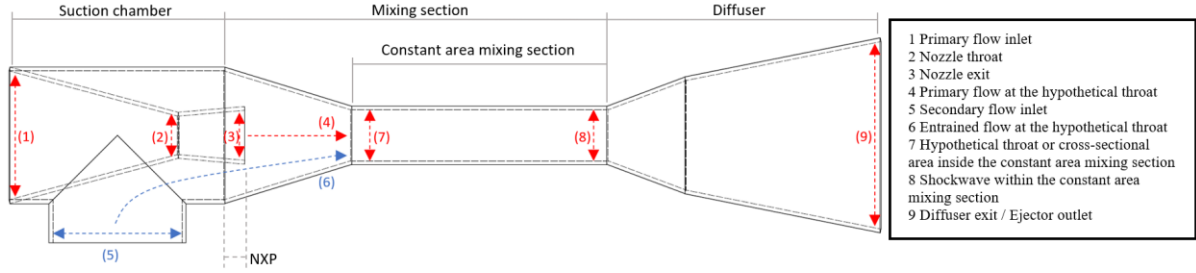
Figure 3.3 Supersonic geoejector designed for Theistareykir Geothermal Field.

3.2.1 Flow regime inside the supersonic geoejector

The primary fluid is accelerated to supersonic speed through the converging-diverging nozzle (from 1 to 3, each number is represented by the location in Figure 3.3), thereby creating underpressure in the mixing section that induces flow from the secondary inlet (5). Ideally, the induced or entrained flow accelerates and reaches sonic speed at the hypothetical throat (6), effectively choking the secondary flow. The primary flow leaving the nozzle is assumed to spread without mixing with the entrained flow (4). The two streams start to mix at the hypothetical throat (7) at constant pressure. The flow remains supersonic within the section until it is compressed and decelerated through a shockwave (8). In reality, a train of shockwaves is formed, but analytical models typically simplify the process and consider one normal shockwave. The flow is then further decelerated in a diffuser (9) to reach a desired back pressure.

3.2.2 Analytical model for the supersonic geoejector

The geometric parameters for the supersonic geoejector were determined using the analytical model. Furthermore, the analytical model was utilized to predict its performance under the specified boundary conditions. The model, like the analytical model for the subsonic geoejector, requires simplifications and assumptions that are necessary to understand the complex flow in the system. The assumptions used in the analytical model are based on the information gathered from the subsonic geoejector field tests and other available literature, primarily Chen et al. (Chen et al., 2017) and Huang et al. (Huang et al., 1999):

1. The flow from both the primary and secondary source is assumed to follow the ideal gas law.
2. The following values, as shown in Chapter 3.1.2, gave an acceptable result in the prediction of outlet pressure and enthalpy of the subsonic geoejector (see Figure 5.4) and will be adapted for the supersonic geoejector:
   a. constant ratio of specific heat (C_p/C_v), $k = 1.327$.
   b. coefficient of frictional and mixing losses, $c_l = 0.84$.
   c. isentropic efficiencies of the nozzle and entrained flow, $\eta_n = 0.90$.
3. The primary flow leaving the nozzle and the entrained secondary flow will not start to mix until they reach the hypothetical throat (location 7 in Figure 3.3).
4. At the hypothetical throat, the two streams start to mix with uniform pressure equal to the pressure of the secondary flow at the hypothetical throat.
5. The entrained flow is choked at the hypothetical throat.
6. The inner walls of the supersonic geoejector are adiabatic.

The following boundary conditions and constraints were added to the model to ensure that the analytical model would meet the requirement in the steamfield for power generation:

1. The exit pressure of the supersonic geoejector should not fall under 9.5 bar-g, or the pressure threshold at the separator, to avoid problems from surges in the steam gathering pipeline.
2. The maximum pressures at the primary and secondary inlet considered in the model are 25 bar-g and 9 bar-g, respectively.
3. The model treats the two-phase flow from well THG-15 as a homogeneous mixture behaving like an ideal gas (i.e. it uses weighted density and enthalpy, and common pressure and temperature). This is a significant simplification given the low quality of the fluid, which raises the importance of phase separation and uncertainty regarding the flow regime. However, at this stage, it is a necessary simplification to get an initial geoejector design.
4. While there is no recent available data to determine the maximum mass flow from THG-15, the mass flow is considered similar to the values in Table 2.1.
5. To ensure that the fluid from the secondary source will be effectively entrained, the pressure of the primary flow at the nozzle exit should be less than or equal to the pressure of the secondary flow at the hypothetical throat.
6. To avoid a shockwave due to sudden change in flow direction, the area of the nozzle exit should be less than the area of the constant area mixing section.
7. The mixture in the constant area mixing section is homogeneous.
8. Effects of the liquid-vapor phase change (i.e. condensation and boiling) are not accounted for in the model.

Following the processes and the assumptions, the analytical model developed to determine the geometric parameters of the supersonic geoejector was largely based on the models developed by Huang et al. (Huang et al., 1999) and Chen et al. (Chen et al., 2017), as shown on Figure 3.4. The thermophysical properties of the fluid were obtained using CoolProp (Bell, I. H., Wronski, J., Quoilin, S., & Lemort, V., 2014).
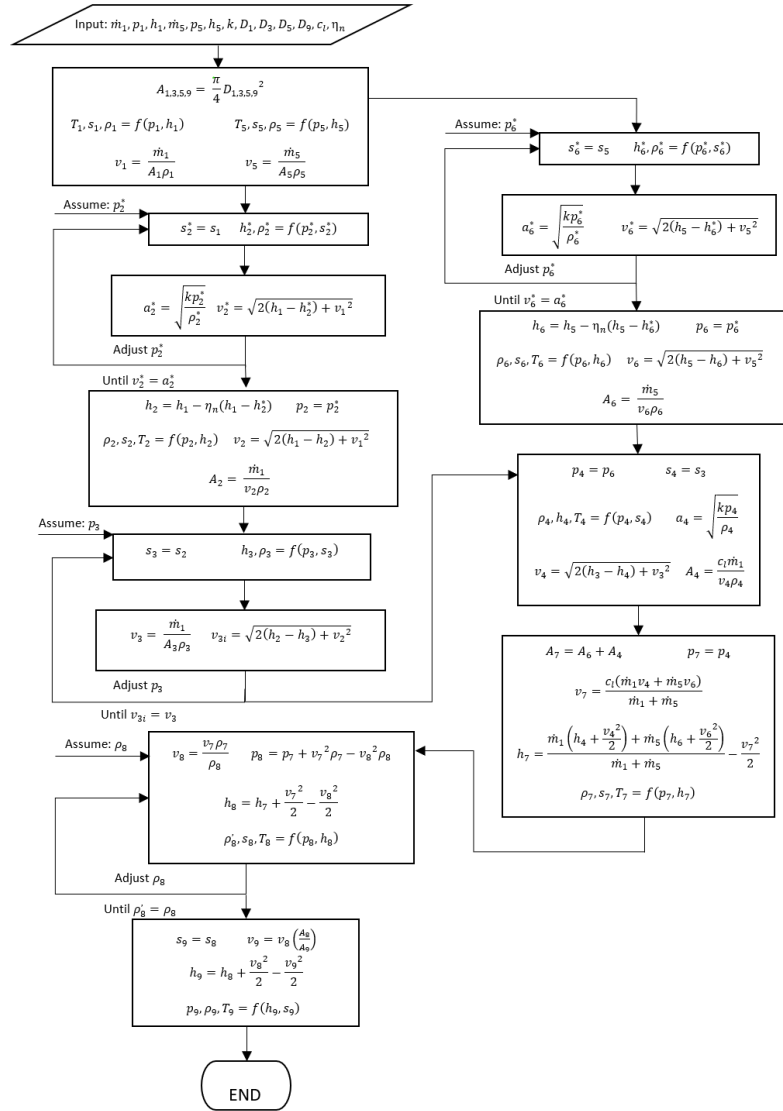
Figure 3.4 Flowchart of the analytical model of the supersonic geoejector.

In this flowchart, as shown in Figure 3.4, the diameters of the primary and secondary inlets, as well as the diffuser outlet, are known; however, the diameter of the nozzle exit must be assumed in order for the model to function. After all other geometric parameters were collected, the diameter of the nozzle exit would be modified to satisfy the constraints. The model requires mass flow, pressure, and enthalpy from the primary and secondary flow inlets as inputs. Following the computations in the flowchart while satisfying the iteration requirements yields the output (pressure and enthalpy at the outlet, as well as geometric parameters). Appendix B contains details on the governing equations of the analytical model's processes. It should be noted that in designing the supersonic geoejector, the inputs in the model should account for the inverse relationship between the mass flow rate and well head pressure of a geothermal well. This is because the calculated nozzle throat area (A_2) and the hypothetical throat (A_7) are the choking points that limit the mass flow rates regardless of the change in the well output.

The flowchart in Figure 3.4 must then be revised algebraically to predict the performance of the supersonic geoejector, with the inputs change to the determined geometric parameters as well as the pressure and enthalpy of the primary and secondary inlets. This modified flowchart will then calculate the outlet's pressure and enthalpy, as well as the

entrainment ratio. This was done because there is no available information to accurately quantify how much flow was entrained from THG-15.

3.2.3 Primary nozzle position and constant area mixing section length

The following geometric parameters of the supersonic geoejector are not directly incorporated within the analytical model, however studies have shown that these parameters have a direct effect to the entrainment ratio and exit pressure:

1. Primary nozzle position (NXP): Distance between the nozzle exit and the entrance of the mixing section or the converging section going to the hypothetical throat (See Figure 3.3). This geometrical parameter is important as it directly impacts the entrainment ratio. NXP will be calculated using the formula presented by Ding et al. (Ding et al., 2016), as shown in Equation 3.1. Where α is an empirical constant that is typically between 0.07 and 0.09. Here, a value of 0.07 is used in the proposed design.

$$NXP = \left(\sqrt{0.083 + 0.76\,ER} - 0.29\right)\frac{D_3}{2^\alpha}$$

(3.1)

2. Length of the constant area mixing section (L_{CAMS}): Studies in the literature have made various conclusions regarding the impact of the length of the constant area mixing section on the entrainment ratio. However, studies showed that as it increases, the mixing effect between the primary and induced flows improves. This efficient mixing decreases the speed differential between the two flows. As a result, the mixed stream becomes more uniform, and the ejector may work at a higher back pressure and gain a higher-pressure ratio. The achievable back pressure, however, declines when the ratio of the L_{CAMS} to its diameter, D_7, exceeds 5 (Chen et al., 2013). With this, a ratio of 5 is used in the current work (see Equation 3.2).

$$\frac{L_{CAMS}}{D_7} = 5$$

(3.2)

These geometrical parameters are based on empirical observations and parameters obtained from the analytical model presented in the previous subsection. Optimizing these geometrical parameters requires experimental validation, which is not covered in this study.

3.3 Energy and exergy analysis

An energy and exergy analysis, in addition to the performance indicators discussed in Chapter 2.4, used to depict the heat and exergy flow inside the geoejector system. Energy analysis is primarily based on the First Law of Thermodynamics, which accounts for the energies entering and exiting the system. Exergy analysis, on the other hand, is based on the Second Law of Thermodynamics, which provides information about the sources and locations of thermodynamic losses (Dincer, I., & Rosen, M. A., 2020).

The system considered for this part of the study is bounded by the primary and secondary inlets up to the geoejector's outlet. Furthermore, to provide a better understanding of the geoejectors' performance, the mixed fluid exiting the geoejector was considered to be separated in its gas and liquid phase at constant pressure at the outlet. This is a significant factor to consider when measuring the performance of geoejectors because the power plant at

Theistareykir Geothermal Field is a single flash power plant and only utilize the separated steam for electricity generation, whereas the separated liquid is currently not utilized.

For the energy analysis, the energy efficiency, η_{energy}, of the geoejector is based on the ratio of the enthalpy flow of the separated steam at the outlet, $\dot{H}_{g(outlet)}$, and sum of the enthalpy flow entering from the primary, $\dot{H}_{primary}$, and secondary inlet, $\dot{H}_{secondary}$, (see Equation 3.3). Additionally, to determine the effectiveness of the geoejector in extracting the energy from the secondary flow, the energy conversion efficiency, $\eta_{\Delta\dot{H}}$, will be calculated based on ratio of the change in useful energy, $\Delta\dot{H}_u$, and enthalpy flow entering from the secondary inlet (see Equation 3.4).

$$\eta_{energy} = \frac{\dot{H}_{g(outlet)}}{\dot{H}_{primary} + \dot{H}_{secondary}}$$

(3.3)

$$\eta_{\Delta\dot{H}} = \frac{\Delta\dot{H}_u}{\dot{H}_{secondary}}$$

(3.4)

For the exergy analysis, the total exergy (E) of a system (see Equation 3.5), in the absence of nuclear, magnetic, electrical, and surface tension effects, is divided into four components: physical exergy (E^{PH}), kinetic exergy (E^{KN}), potential exergy (E^{PT}), and chemical exergy (E^{CH}) (Bejan et al., 1996).

$$E = E^{PH} + E^{CH} + E^{KN} + E^{PT}$$

(3.5)

Only kinetic and physical exergy were considered for geoejector systems, and the rest are negligible. To simplify the calculation of exergy in each component of the geoejector, the total specific exergy (e) on a mass basis for the geoejector shall be calculated using Equation 3.6-3.8.

$$e = e^{PH} + e^{KN}$$

(3.6)

Where:

$$e^{PH} = (h_k - h_0) - T_0(s_k - s_0)$$

(3.7)

$$e^{KN} = \frac{V_k^2}{2}$$

(3.8)

In this part of the study, the subscripts k and 0 represent the component and environmental or dead state, respectively. The environmental state taken into account was based on the available average temperature at one of the nearby meteorological stations, Husavik, during the month of September when the field tests were conducted. The average environmental state employed in this analysis is 6.3 °C (Climate-Data.org, 2023) and the ambient pressure is assumed to be 1 bar.

To determine the exergetic efficiency or effectiveness of the geoejector system, ϵ_k, an exergy rate balance should be performed to calculate the exergy rate of destruction and loss in the stream (see Equations 3.9-3.11).

$$\epsilon_k = \frac{\dot{E}_{p,k}}{\dot{E}_{f,k}} = 1 - \frac{\dot{E}_{d,k} + \dot{E}_{l,k}}{\dot{E}_{f,k}}$$

$$\text{(3.9)}$$

$$\dot{E}_{f,k} = \dot{E}_{p,k} + \dot{E}_{d,k} + \dot{E}_{l,k}$$

$$\text{(3.10)}$$

Where:

$$\dot{E}_k = \dot{m}_k e_k$$

$$\text{(3.11)}$$

The exergy rate of component associated with the fuel, $\dot{E}_{f,k}$, refers to the exergy coming from the primary and secondary inlet, while the exergy rate of component associated with the product, $\dot{E}_{p,k}$, refers to the exergy stream of the separated steam in the outlet. The exergy rate of loss of component, $\dot{E}_{l,k}$, refers to the exergy stream of the separated liquid in the outlet. The exergy rate of destruction of components, $\dot{E}_{d,k}$, refers to the exergy destroyed in the stream.

Chapter 4

Numerical modelling for subsonic and supersonic geoejector

For this study, a commercial CFD software (ANSYS CFX) was used for the numerical modelling to discretize the governing differential equations (continuity, momentum, and total energy) within the geoejector. ANSYS CFX has an advanced coupled solver with powerful preprocessing and post processing features that is capable of modelling steady-state, turbulent flows, subsonic and supersonic flows, and multiphase flows (ANSYS Inc., 2023a). These ANSYS CFX features are necessary for the numerical modelling of the geoejectors.

In this study, it is important to note that a large relative inaccuracy of the numerical model in comparison to experimental data is possible. To reduce this inaccuracy, model complexity must be increased, which necessitates more information about the flow conditions (i.e. local pressures, velocity profiles, turbulence intensity, and vapor quality) (Ringstad et al., 2020). Furthermore, because the flows within the geoejector are complex, the model must be simplified to decrease the high computational cost. Despite this, numerical modeling is crucial because it can provide information on the underlying transport phenomena for heat, momentum, and mass transfer.

This chapter will discuss the parameters used for the numerical modelling of the subsonic and supersonic geoejector.

4.1 Geometry and mesh

As the findings of this study are intended to be used at Theistareykir Geothermal Field for additional research and field testing, the geometrical parameters of the subsonic and supersonic geoejectors will not be given at this point. Nevertheless, Figure 4.1 shows the geometry and mesh of the geoejectors used in this study. The figure shows that the geometry's outlet is far from the diffuser's end. This is an important consideration to ensure that the thermophysical parameters of the mixed fluid at the exit are uniform across the cross-sectional area of the outlet.
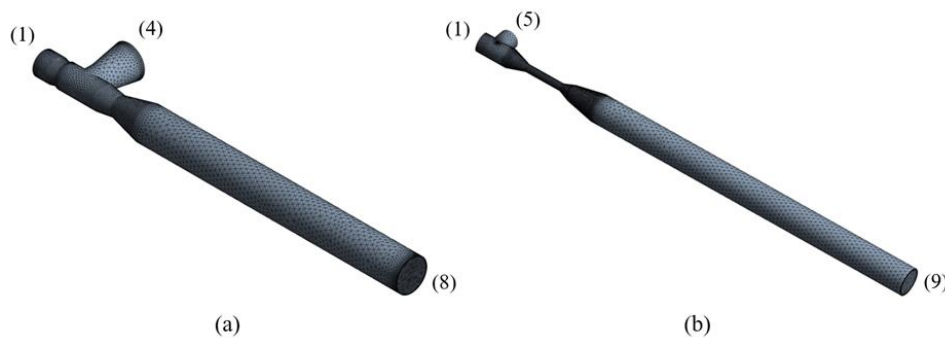
Figure 4.1 Geometry and mesh of (a) subsonic geoejector (b) supersonic geoejector.

Each number is represented by the location in Figure 3.1 and 3.3 for the subsonic and supersonic geoejector, respectively. Note that the figures were not scaled.

To improve results accuracy and minimize convergence issues, both geoejector meshes in Figure 4.1 (a and b) were built using the mesh matrix criteria as shown in Table 4.1. A grid convergence study was performed in order to measure the variance of the computed solution and reduce the computational time when using different grid sizes (see Appendix C). Both subsonic and supersonic geoejectors were analyzed in three levels of grids (coarse, fine, and very fine) and the variations of calculated results in several measure points (a. Subsonic geoejector: static pressure at the primary and secondary inlet, and enthalpy at the outlet; b. Supersonic geoejector: mass flow rate at the primary and secondary inlet and enthalpy at the outlet).

Table 4.1 Mesh matrix for subsonic and supersonic geoejector.

Description	Measures of mesh quality	Subsonic geoejector	Supersonic geoejector
No of Nodes		51 449	96 023
No of Elements		135 686	245 199
Aspect ratio	• The acceptable range is less than 1000 if running double precision. [1]	Min: 1.1727 Max: 79.5140 Average: 8.3798	Min: 1.1616 Max: 37.112 Average: 4.1756
Skewness	• 0 (ideal) to 1 (worst).[2] • Should be less than 0.95 to avoid convergence difficulties. [2]	Min: 0.0003 Max: 0.9181 Average: 0.2022	Min: 0.0001 Max: 0.9309 Average: 0.2242
Orthogonal quality	• 0 (worst) to 1 (ideal).[2] • Orthogonal factor should be greater than $\frac{1}{3}$.[1]	Min: 0.08194 Max: 0.9901 Average: 0.7957	Min: 0.06907 Max: 0.9913 Average: 0.7746

[1](ANSYS Inc., 2023b), [2](ANSYS Inc., 2023d)

4.2 CFD settings

4.2.1 Numerical scheme

The flow domain of the model is a three-dimensional steady state with advection scheme and turbulence numerics set in high resolution. In high resolution setting, it enforces a boundedness criterion by varying the blend factor values across the domain according to the local solution field. Blend factor will be close to 1.0 for accuracy in the flow region with low variable gradients and close to 0.0 in regions with abrupt changes in the variable gradients to prevent overshoot and undershoot and to maintain robustness. The blend factor of the advection scheme 0.0 is similar to first order scheme and blend factor 1.0 is similar to second order scheme (ANSYS Inc., 2023b).

4.2.2 Turbulence model

There are several turbulence models used to predict the ejector flow, however the results have not been conclusive as to which model gives the most accurate prediction (Djajadiwinata et al., 2021). From the study conducted by Zhu et al. (Zhu, Y., & Jiang, P. 2013), four

turbulence models (Standard k-epsilon, Realizable k-epsilon, Renormalization-group (RNG) k-epsilon, and Shear stress transport k-omega model) in three-dimensional ejector were compared in the experimental data. The results found that the RNG k-epsilon model provides the most accurate predictions of both shockwave structures and mass flow rates.

The RNG k-epsilon model was used in this study to simulate the flow regime of the geoejector. This turbulence model is based on renormalization group analysis of the Navier-Strokes equations, where the standard k-epsilon model's transport equations for turbulence generation and dissipation are same, but the model constants are different. For more information about the turbulence model, see ANSYS Inc., 2023c.

4.2.3 Materials

The geothermal fluid has a wide variation in chemical composition between and within geothermal fields, and, in some cases, over time within the same geothermal wells (Clark et al., 2011). To simplify the model, the fluid coming from the primary and secondary inlets is assumed to have the properties of pure water. Furthermore, in the field setup, the fluid flowing from the primary inlet is considered dry steam and presumed to be at saturation vapor point, but the fluid entering from the secondary inlet is wet steam with a steam quality of 8-10% (varies depending on the inlet pressure).

In this study, the material or fluid in the system is set to homogeneous binary mixture of saturated liquid and vapor of wet steam. The material uses the IAPWS 97 database (Wagner, W., & Kruse, K., 1998) to determine the equation of state for water and steam properties.

4.2.4 Boundary conditions

The configuration of boundary conditions determines the robustness of the solution. For the subsonic geoejector, the configuration of the boundary conditions was set to "most robust" or most stable configuration. The boundary conditions of the model were mass flow rate, total temperature, and steam quality at the primary and secondary inlet, as well as static pressure at the outlet. This configuration for the subsonic geoejector was used to calculate the static pressure from the primary and secondary inlet, as well as the enthalpy at the outlet.

For the supersonic geoejector, the configuration of the boundary condition was set to "sensitive to initial guess". The inputs of the model were total pressure, total temperature, and steam quality at the primary and secondary inlet, as well as static pressure at the outlet. This configuration for the supersonic geoejector will calculate the mass flow rate from the primary and secondary inlet, as well as the enthalpy at the outlet.

In comparison to the subsonic geoejector, the supersonic geoejector configuration is less robust. Nonetheless, this configuration was chosen because there is no measured data available to quantify the amount of entrained fluid from the secondary flow for the supersonic ejector.

4.2.5 Convergence criteria

The simulation ran iterations at each timestep to converge its residuals to below a target of 1×10^{-6}. However, simulation shows a transient convergence behavior wherein the target residual levels could not be obtained due to an inherent unsteadiness of the solution. To reduce the computation time of the simulation, the following constraints were used to determine whether the subsonic or supersonic geoejector solution converged:
1. The simulation should have at least 100 iterations.

2. Changes in the measure points should be minimal from the previous 100 iterations. The measure points added in the model are as follows:
    a. Subsonic geoejector: static pressure at the primary and secondary inlet, as well as enthalpy at the outlet.
    b. Supersonic geoejector: mass flow rate at the primary and secondary inlet, as well as enthalpy at the outlet.
3. The energy, mass, and momentum imbalance should be less than 0.5%.

Chapter 5

Results and discussion

5.1 Subsonic geoejector

Using the available field measurements, the overall performance of the subsonic geoejector during the field test was determined (See Figure 5.1). It is important to note in this data that the field test does not run continuously, and there is a gap between September 02 and September 08, 2021.
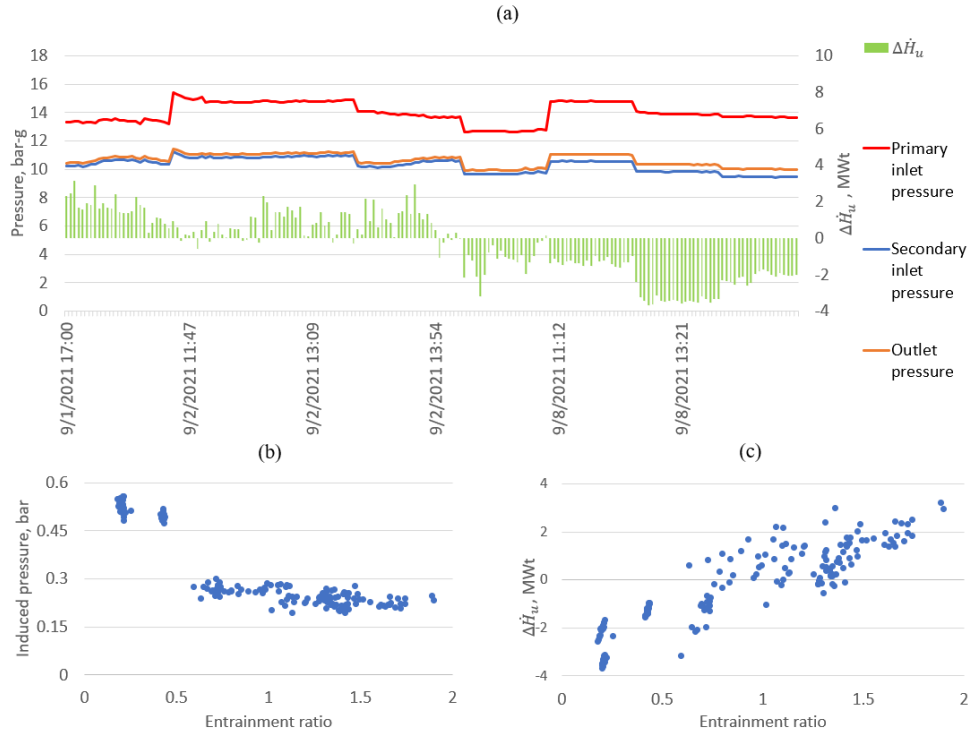
Figure 5.1 Overview of the performance of the subsonic geoejector.

The pressure readings in Figure 5.1(a) reveal that the subsonic geoejector successfully increased the pressure of the entrained flow from the secondary inlet by up to 0.55 bar. These higher induced pressure levels were obtained on September 8th when the secondary flow was curbed. As illustrated in Figure 5.1(b), the lower the entrained fluid from the secondary flow, the higher the induced pressure. It is believed that when the entrained mass flow decreases, more available energy from the primary flow is transferred to the entrained flow.

The change in useful energy, $\Delta \dot{H}_u$, in Figure 5.1(a) shows that the majority of the positive results were obtained during the field test from September 1 to 2, whereas the majority of the negative results were obtained during the field test from September 8. This could have occurred because the procedures used during these field test periods were different. The negative $\Delta \dot{H}_u$ is believed to be caused by the restriction in the flow from the secondary inlet, resulting to a lower entrained flow. This was also seen in Figure 5.1(c), where a smaller entrainment ratio

led to a lower or negative $\Delta\dot{H}_u$. It is believed that the difference in speed between the primary and secondary streams at the mixing chamber have risen as entrained flow dropped, resulting in a higher shear stress and mixing losses. This could not be verified using field test measurements due to a lack of information beyond the secondary inlet. Futher analysis on this is discussed in the results of the numerical model.

To further understand the field test measurements, the analytical model was used to analyze and illustrate the flow regime inside the subsonic geoejector with pressure-enthalpy (Ph) diagram and pressure and velocity profile of Case No. 090221_1140 (Case number indicates to the date and time of the field test. Analytical model inputs: $\dot{m}_1$=8.45, $\dot{m}_4$=12.49 kg/s, p_1 =15.40 bar-g, p_4=11.24 bar-g, h_1=2787 kJ/kg, and h_4=950 kJ/kg), as shown in Figure 5.2 and Figure 5.3, respectively.
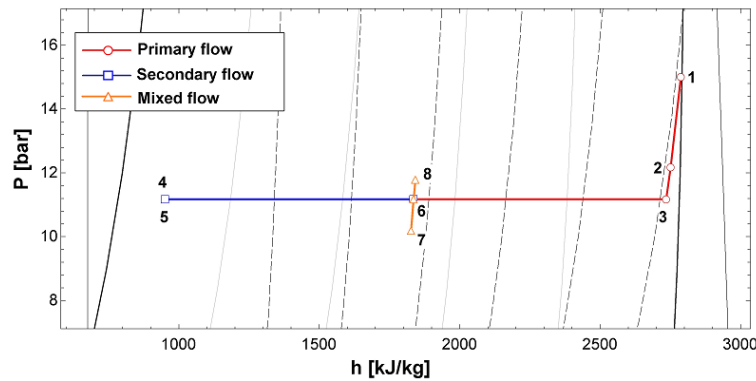
Figure 5.2 Calculated ph diagram of the subsonic geoejector from the analytical model (each point is represented by the location in Figure 3.1).
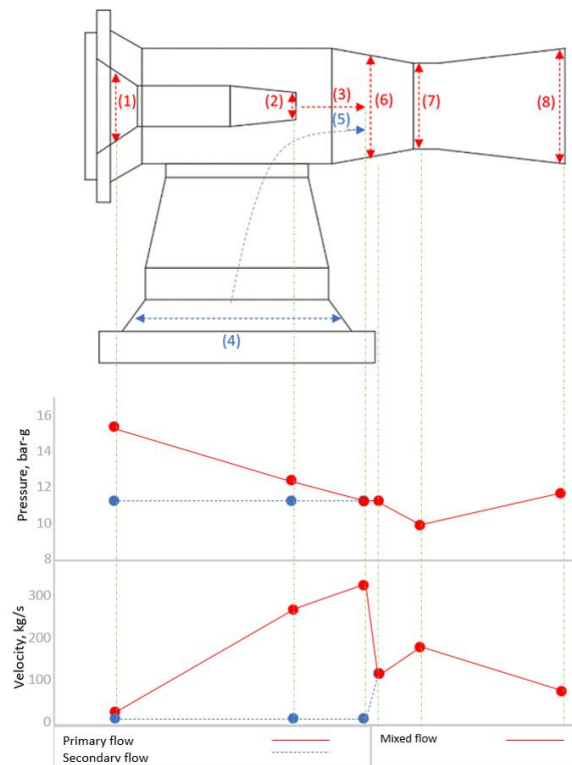

Figure 5.3 Calculated pressure and velocity profile of the subsonic geoejector from the analytical model.

Figures 5.2 and 5.3 show that the nozzle accelerates the primary fluid from 17.39 to

266.99 m/s (point 1 to point 2, each number is represented by the location in Figure 3.1). This acceleration reduced the primary flow's pressure from 15.40 to 12.40 bar-g. However, the pressure of the primary flow leaving the nozzle remains higher than the pressure of the secondary flow, 11.24 bar-g (5) which could not have led to entrainment of the secondary flow. It is believed that the underpressure was created further downsteam (3) as the field test measurements show that the subsonic geoejector did entrain flow from the secondary flow based on these conditions. As the fluid mixed in the mixing section (6), the mixture was assumed to be homogeneous with pressure, velocity, and enthalpy of 11.24 bar-g, 111.23 m/s, and 1685.25 kJ/kg, respectively. The mixed fluid was then accelerated as it passed through the throat and resulted in a reduction of pressure to 9.88 bar-g (7). Finally, as the fluid decelerated in the diffuser, pressure recovered, yielding pressure and enthalpy of 11.65 bar-g and 1689.3 kJ/kg, respectively (8). The output pressure and enthalpy of the analytical model shows a good agreement with the field test measurement in the outlet that gives relative error of 1.64% and 1.01%, respectively.

The results were compared to field test measurements to validate the analytical model, as shown in Figure 5.4. The chart shows a good agreement between the results and field measurements with a maximum relative error of 13.01% for static pressure and 10.37% for enthalpy at the outlet. The majority of the high relative errors were detected during the September 8 field test. This is believed to be related to the observations found in the field test measurements were negative $\Delta \dot{H}_u$ is obtained.
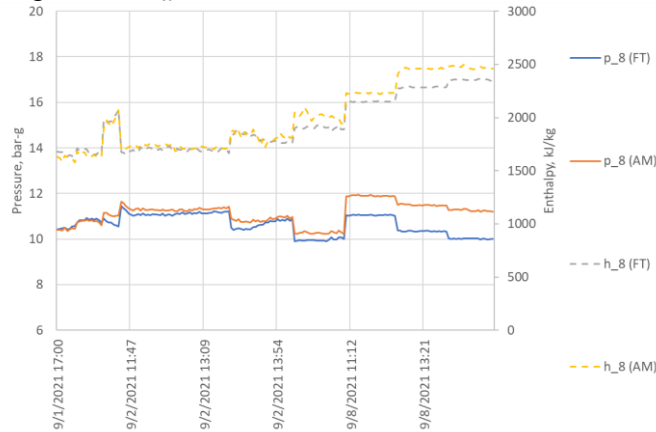
Figure 5.4 Validation of analytical model (AM) with field test (FT) measurements for subsonic geoejector.

With the information obtained from the analytical model, the Sankey and Grassman diagram (see Figure 5.5) were used to visualize the energy and exergy flow within the system. In the diagrams, the height of the box represents the amount of (a) energy and (b) exergy within the system. In the Sankey diagram in Figure 5.5(a) shows that the subsonic geoejector has an energy efficiency, η_{energy}, of 73.35%. Additionally, it was found that the energy conversion efficiency, $\eta_{\Delta \dot{H}_u}$, or the percentage of energy absorbed from the secondary flow to the separated steam outlet of the subsonic geoejector is 20.42%. On the other hand, in Figure 5.5(b), the exergetic efficiency, ϵ_k, was determined to be 72.21%. Further, the Grassman diagram shows that most of the exergy destruction occurred when the primary and secondary streams mixed, for this case the exergy destruction during mixing was 1.69% of the total exergy.

(a)

(b)
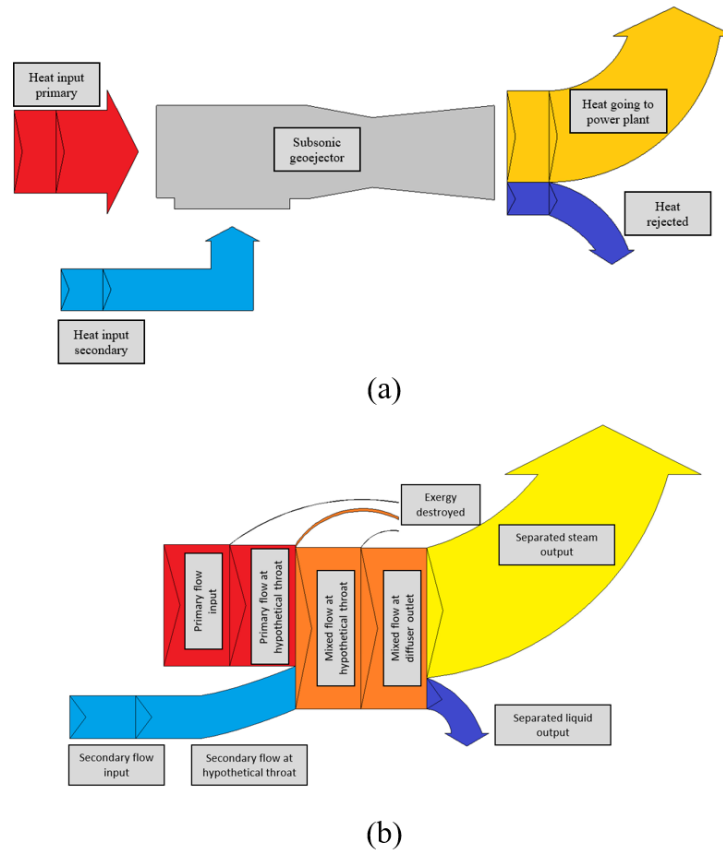
Figure 5.5 (a) Sankey and (b) Grassman diagram of the subsonic geoejector from the results of the analytical model for Case no. 090221_1140.

The analytical model provides information about the flow regime inside the subsonic geoejector; nevertheless, a numerical model is required to identify the underlying transport phenomena for heat, momentum, and mass transfer. Figure 5.6 shows the pressure, velocity, and enthalpy profile of the Case no. 090221_1140 obtained from the numerical model (Numerical model inputs: $\dot{m}_1$=8.45, $\dot{m}_4$=12.49 kg/s, T_{1-0}=202.6 °C, T_{4-0}=188.86 °C, x_1=1, x_4=0.075, and p_8=11.46 bar-g).

(a)

(b)

(c)
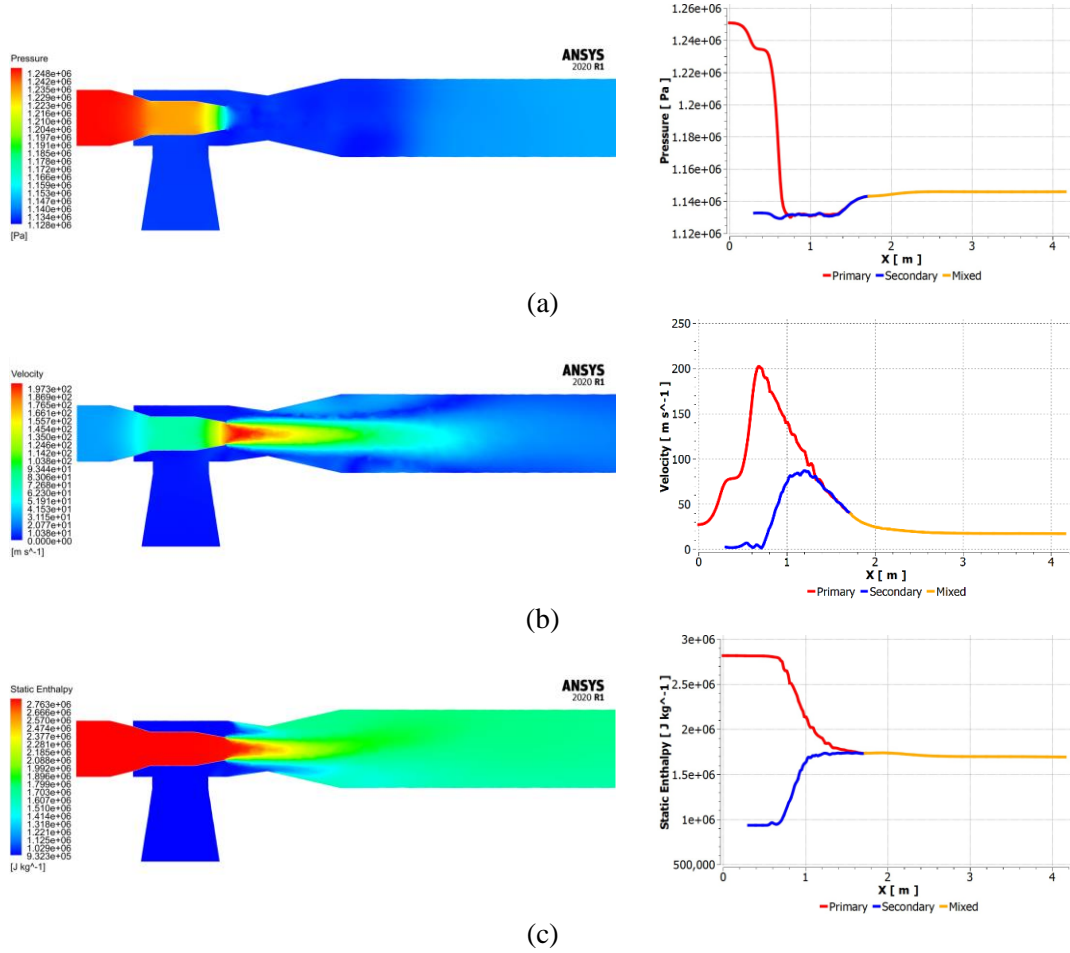
**Figure 5.6 Calculated (a) pressure, (b) velocity, and (c) enthalpy profile of case no. 090221_1140 from the numerical model.**

In Figure 5.6, the primary flow at a pressure of 12.51 bar-g was accelerated in the nozzle to 176.31 m/s, resulting in a pressure reduction to 11.61 bar-g. The figure shows that the pressure of the primary flow leaving the nozzle continues to decrease and is accelerated further in the mixing section. This acceleration of the primary fluid produced an underpressure of 11.32 bar-g, which allowed entrainment to the secondary flow. Unlike the assumption in the analytical model, the stream did not immediately mix at the mixing section, as seen in Figures 5.6 (b) and (c). Furthermore, because the minimum length was not present at the mixing section's throat, both streams did not properly mixed until they were further downstream of the outlet of the geoejector. The exit pressure and enthalpy of the fully mixed streams were 11.46 bar-g and 1694.37 kJ/kg, respectively. In comparison to the field test measurements, the primary pressure inlet had the biggest relative error of 23.06%. While the secondary inlet pressure and outlet enthalpy exhibit good agreement with relative errors of 1.72% and 3.38%, respectively.

The resulting pressure, velocity, and enthalpy profiles of the analytical and numerical model for Case no. 090221_1140 were plotted together to determine the difference between the analytical and numerical model outputs (see Figure 5.7). The figure shows that there were two key disparities between the profiles. First, the pressure projected by the numerical model is lower than the pressure measured in the field, which was also used as input for the analytic model. However, both the analytical and numerical models demonstrate that the primary flow generated an underpressure downstream of the nozzle, allowing entrainment from the

secondary flow. Second, the numerical model result showed that the streams mixed further downstream of the diffuser, contrary to the analytical model's assumption that the streams mixed instantaneously at the mixing section.
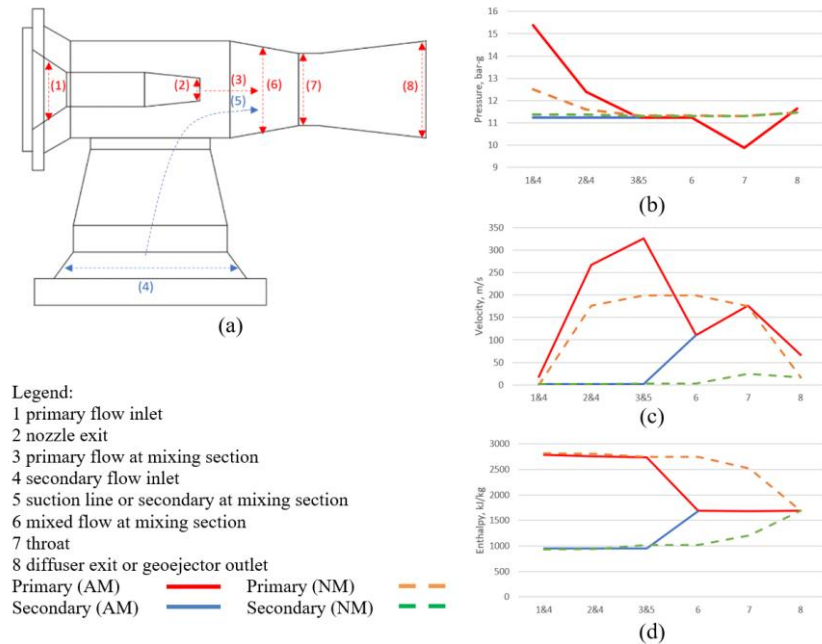
Figure 5.7 Predicted flow regime for the subsonic geoejector from the analytical (AM) and numerical (NM) model. (a) schematic diagram of subsonic geoejector with reference points; (b) pressure profile; (c) velocity profile, and (d) enthalpy profile.

The results of the analytical and numerical models were compared to determine their accuracy in predicting the field test measurement, as shown in Figure 5.8. Unfortunately, because the models have different output (pressure and enthalpy at the outlet for the analytical model, and pressure at the primary and secondary inlet, as well as enthalpy at the outlet for the numerical model), they could not be directly compared. The figure demonstrates that the analytical model agrees better with the field test measurements (with a maximum relative error of 13.01% at the outlet pressure) than the numerical model (with a maximum relative error of 23.80% at the primary inlet pressure).
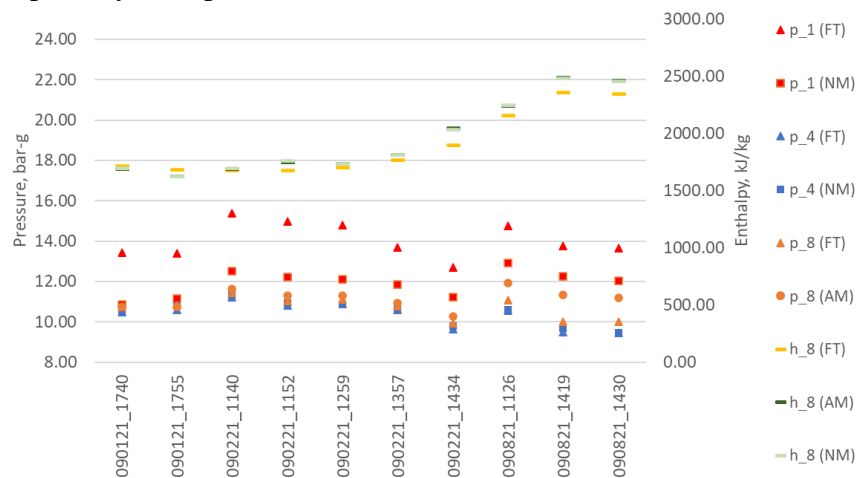
Figure 5.8 Comparison of field test measurements (FT), analytical model (AM), and numerical model (NM).

To further understand the factors that affect the performance of the subsonic geoejector, an analysis on the shear stress generated due to the difference in speed between the primary and secondary streams at the mixing section was performed. It seems that during the September 8 field test, the shear stress induced by the increased mass flow from THG-11 is higher than that of the September 2 field test (see Figure 5.9). This increased shear stress is thought to have increased mixing losses in the stream during the September 8 field test. This phenomenon was also observed in the analytical model of the subsonic geoejector. The agreement of the field test measurements and the analytical model for the September 8 data improved when the model's losses were increa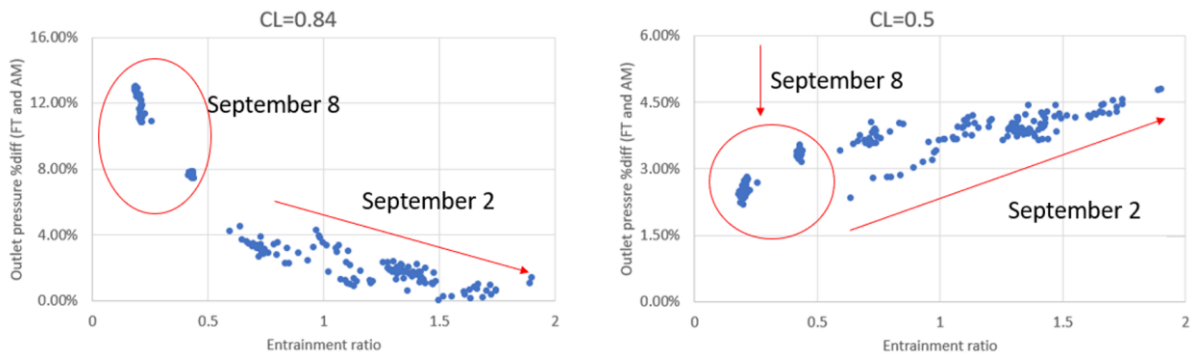sed (c_l from 0.84 or 16% loss to 0.5 or 50% loss), but there was an increase in relative error for the September 1-2 data (see Figure 5.10).
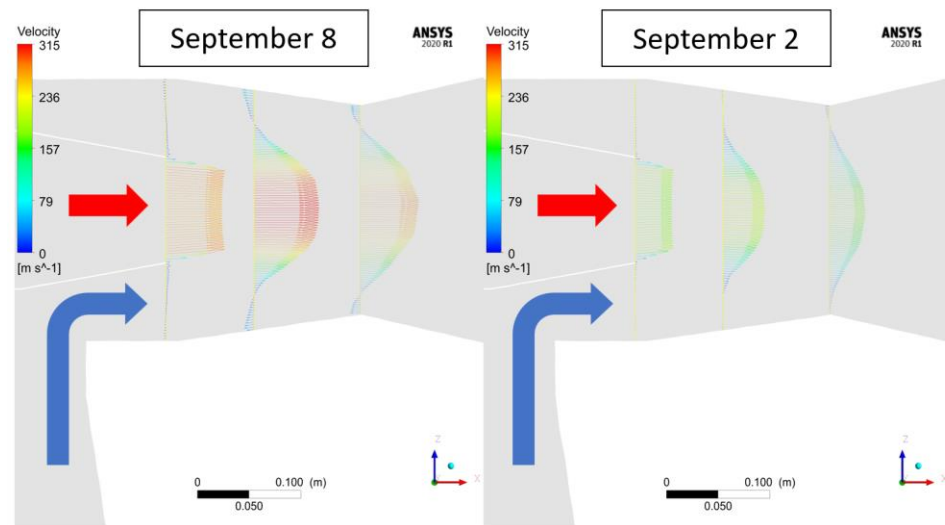
Figure 5.9 Shear layer between the primary (coming from the red arrow) and secondary (coming from the blue arrow) stream at the mixing section.

Figure 5.10 Comparison of results between the field test (FT) and analytical model in varying coefficient of loss.

Regardless of how well the subsonic geoejector performed in the field test, the information gained from the analytical and numerical models indicates that the subsonic geoejector could not be used when the high-pressure geothermal well, THG-11, is run at its normal operating pressure. This is because the acceleration of the primary fluid in the nozzle is insufficient, resulting in a pressure leaving the nozzle that is too high (i.e. for a primary inlet pressure of 25 bar-g, the nozzle exit pressure is estimated to be 17.57 bar-g) to allow entrainment from the secondary flow and could generate a backflow in the secondary inlet due to a high-pressure difference at the mixing section. Lastly, a narrower and longer throat at the

mixing section is needed to improve the mixing effect of the primary and secondary streams and to reduce mixing losses caused by considerable differences in speed between the streams.

5.2 Supersonic geoejector

The supersonic geoejector was designed to solve the anticipated issues in using the subsonic geoejector under the THG-11's normal operating conditions. Because this study is regarded as a first step toward building a practical and cost-effective geoejector, the acquired geometric parameters from the analytical model were changed to standard pipe sizes that are commercially available in order to reduce the cost of the planned field test. However, because the geoejector study is still ongoing and a field test is being prepared, the geometric parameters acquired are not included in this study. Still, the results for the supersonic geoejector's operating parameters, flow regime, and performance will be provided and discussed in this chapter.

To estimate the operational range of the supersonic geoejector, as shown in Figure 5.11, the geometrical parameters obtained were used in the analytical model while varying inlet pressure for the primary and secondary inlets.
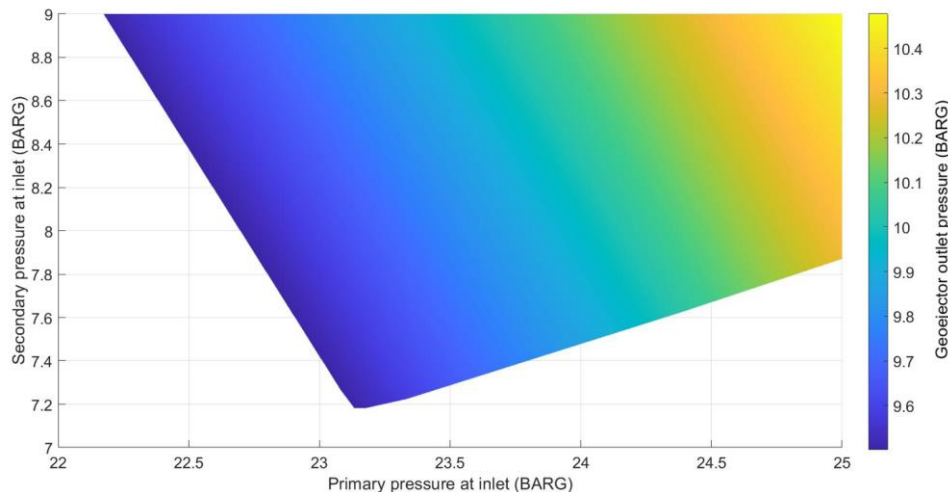
Figure 5.11 Geoejector exit pressure for varying input pressures.

Figure 5.11 shows that the induced pressure ranges from 0.5 to 2.4 bar. As the pressure from the primary flow varies, there is a corresponding minimum pressure that the secondary flow should meet to ensure that the output of the geoejector is not susceptible to surges in the steam gathering system. This sets the operational range of the geoejector. When the pressure from the primary flow is lower than 23.1 bar-g, there is a need to increase the pressure from the secondary flow. This is needed because as the pressure at the primary flow inlet decreases, so does the primary mass flow rate, reducing the available energy from the primary flow to increase the pressure of the entrained flow. Furthermore, if the primary inlet pressure falls below 22.2 bar-g, the energy from the primary flow will not be enough to induce flow from the secondary inlet while reaching the desired minimum outlet pressure and therefore the geoejector cannot be run at such condition. Changes in the geometric parameters of the geoejector are required to handle lower than 22.2 bar-g inlet pressure of the primary flow. However, this would limit the mass flow from THG-11 and decrease its power output. On the other hand, when the pressure from the primary flow is greater than 23.1 bar-g, there is still a need to increase the pressure from the secondary flow. This increase is necessary to be certain that the pressure of the secondary flow in the hypothetical throat remains higher than the

pressure of the primary flow leaving the nozzle. This scenario can be observed in Figure 5.12.
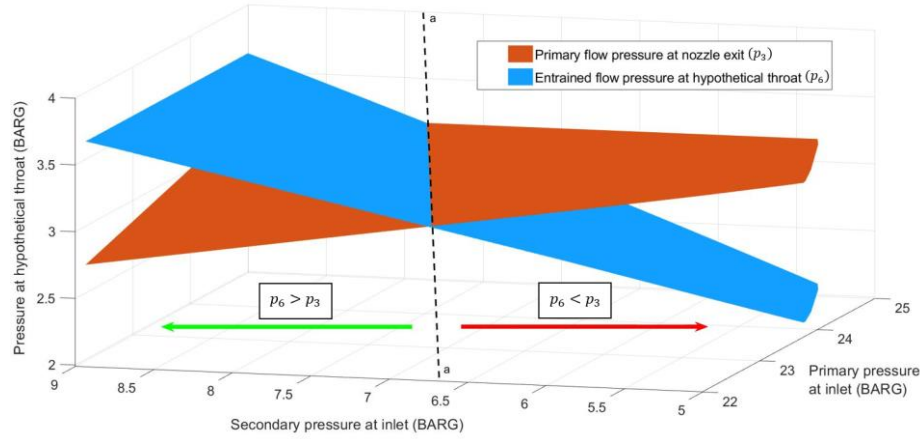

Figure 5.12 Pressure of primary flow at nozzle exit and entrained flow at the hypothetical throat.

Figure 5.12 shows that the area to the right of line a-a is where the primary flow pressure at the nozzle exit (p_3) is greater than the pressure from the entrained flow at the hypothetical throat (p_6). If the geoejector operates at this condition the entrainment ratio is expected to decrease due to unfavorable pressure difference. This area could be reduced by increasing the diameter of the nozzle exit to decrease the primary flow pressure even further. However, as mentioned in the constraints in Chapter 3.2, the area of the nozzle exit should not be greater than the area of the constant area mixing section.

The relationship between the induced pressure of the secondary flow and entrainment ratio is shown in the upper portion of Figure 5.13. When induced pressure is at its lowest, 0.5 bar, the entrainment ratio is at maximum, 50.4%. On the other hand, if the induced pressure is at maximum, 2.4 bar, the entrainment ratio will be at lowest, 25.8%. This range of entrainment ratio and induced pressure is ideal as the values obtained for the mass flow for both wells are near their maximum, see the lower graph of Figure 5.13. Note that the areas plotted in this figure are determined by the operational range shown in Figure 5.11.
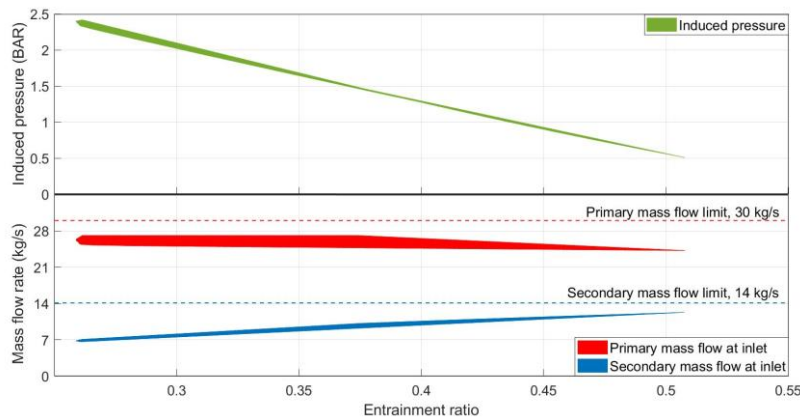
Figure 5.13 Induced pressure and mass flow vs entrainment ratio.

To further understand the flow regime inside the supersonic geoejector, the predicted performance in the operating condition provided by the field operators (Analytical model inputs: p_1=25 bar-g, p_5=9 bar-g, h_1=2802 kJ/kg, and h_5=950 kJ/kg) is illustrated with pressure-enthalpy (Ph) diagram and pressure and Mach No. profile as shown in Figure 5.14 and 5-15, respectively.
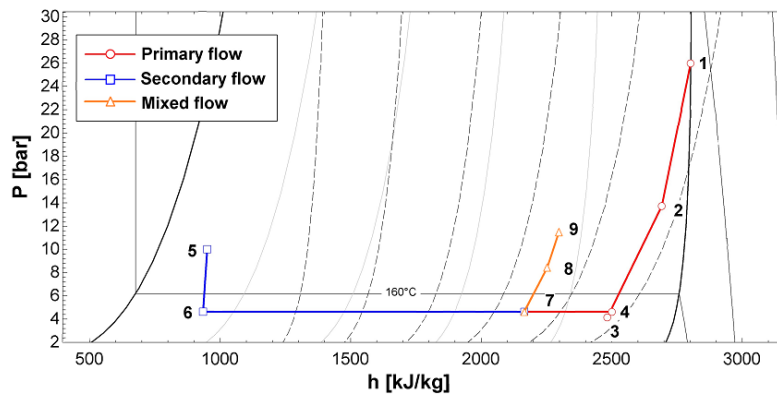
Figure 5.14 Calculated ph diagram of the supersonic geoejector from the analytical model (each step is represented by the location in Figure 3.3).
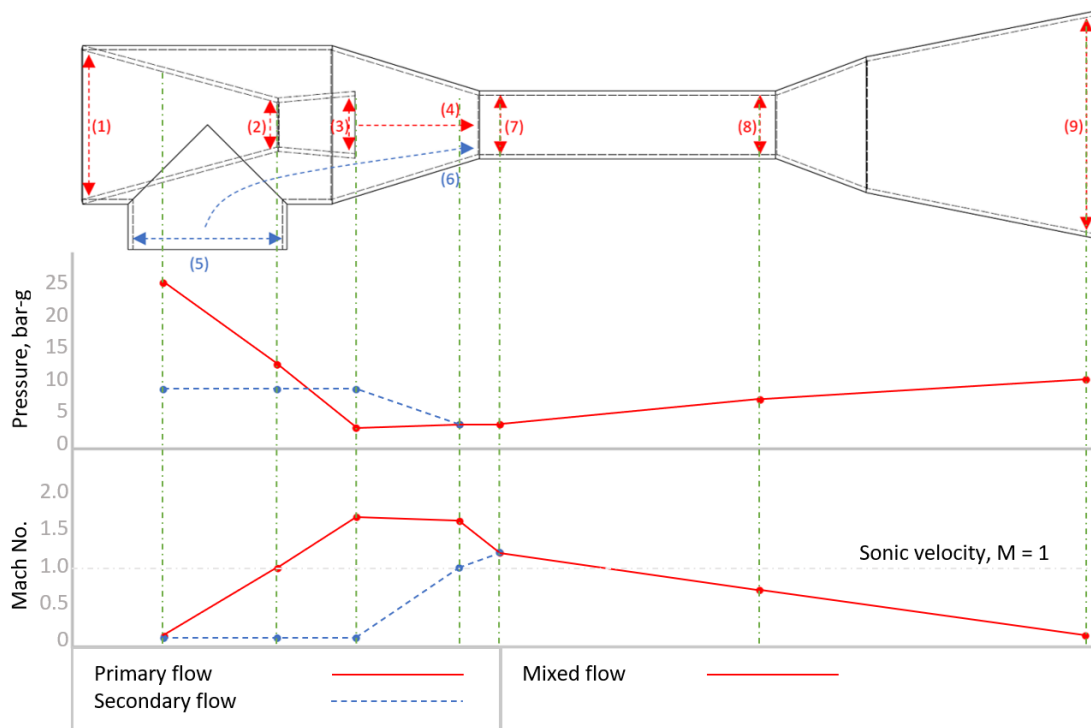
Figure 5.15 Calculated pressure and Mach No. profiles of the supersonic geoejector from the analytical model.

The nozzle accelerated the primary fluid to supersonic speed at Mach No. 1.72 (3, each point indicated by the location in Figure 3.3) and created an underpressure of 3.17 bar-g, as shown in Figures 5.14 and 5.15. Because of this underpressure, the secondary flow was entrained and choked at the hypothetical throat, resulting in acceleration to Mach No. 1 and pressure decrease to 3.64 bar-g (6). The two streams were considered to be homogeneous as they mixed in the hypothetical throat (7), with pressure, Mach No., and enthalpy of 3.64 bar-g, 1.22, and 2164.13 kJ/kg, respectively. The mixed fluid is decelerated to Mach No. 0.69 by a shockwave (8) as it travels through the constant area mixing section, which raises the pressure to 7.41 bar-g. The flow is then decelerated further in the diffuser (9) to achieve pressure and enthalpy values of 10.48 bar-g and 2297.10 kJ/kg, respectively. The analytical model yielded mass flow rates of 27.11 and 10.16 kg/s for the primary and secondary flow, respectively.

With the information obtained from the analytical model, the Sankey and Grassman

diagram (see Figure 5.16) were used to visualize the energy and exergy flow within the system. In the diagrams, the height of the box represents the amount of (a) energy and (b) exergy within the system. In the Sankey diagram in Figure 5.16(a), it shows that the supersonic geoejector has an energy efficiency, η_{energy}, of 91.62%. Additionally, it was found that the energy conversion efficiency, $\eta_{\Delta \dot{H}_u}$, or the percentage of energy absorb from the secondary flow to the separated steam outlet of the subsonic geoejector was 25.67%. On the other hand, in Figure 5.16(b) the exergetic efficiency, ϵ_k, is 86.62%. Further, the Grassman diagram shows that most of the exergy destruction occurred when the primary and secondary streams mixed at the constant area mixing section, for this case the exergy destruction during mixing was 7.21% of the total exergy. The increased in exergy destruction in this part of the geoejector was the result of the added coefficient of frictional and mixing losses in the model.
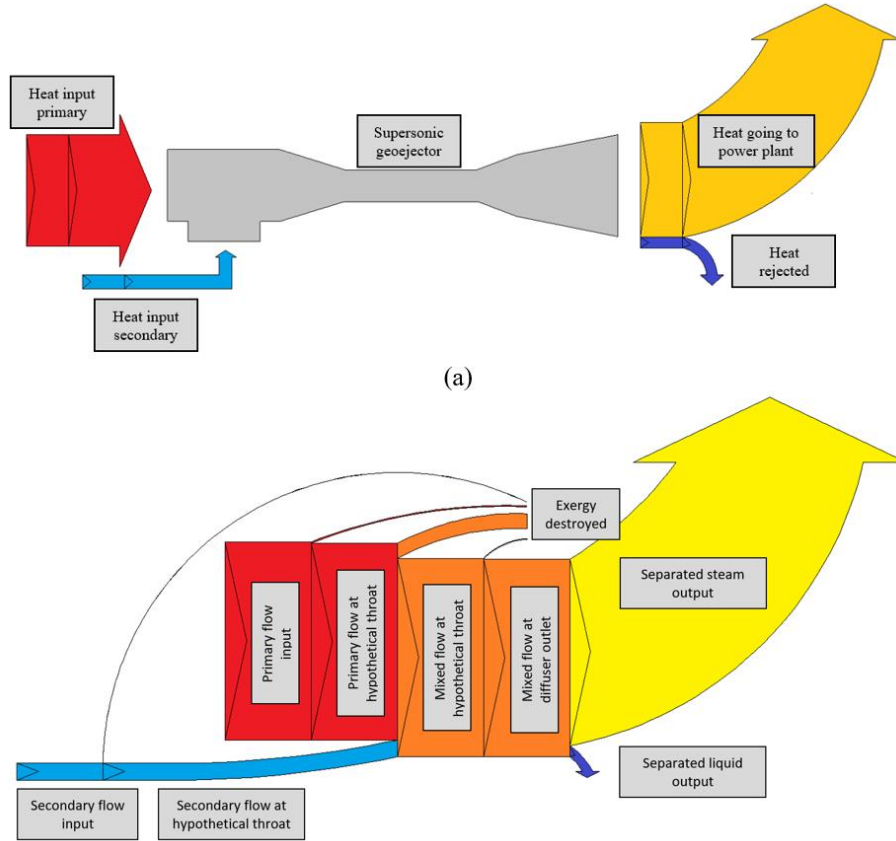
Figure 5.16 (a) Sankey and (b) Grassman diagram of the supersonic geoejector from the results of the analytical model.

Since the supersonic geoejector is planned to be connected to the power plant, the change in power output under the operational range (see Figure 5.11) was compared to the generated power from only using well THG-11 (without geoejector), as shown in Figure 5.17.
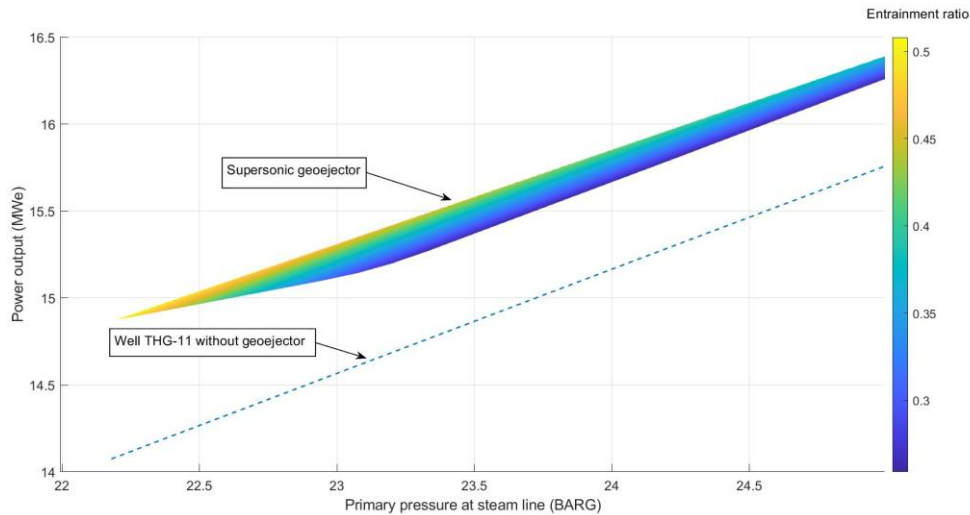
Figure 5.17 Power output potential from using supersonic geoejector and from well THG-11 only (without geoejector).

The result of the model, from Figure 5.17, suggests that the added power generation from the supersonic geoejector could vary from 0.5 to 0.8 MWe or 25% to 40% of the wellhead potential of THG-15. The figure further shows that the highest added power output from THG-15 is only achievable when the output from THG-11 is limited, however, the total power output declines as the input from THG-11 is reduced (entrainment ratio increases). Note that the variation in the power output of the supersonic geoejector is dependent on the inlet pressures of both primary and secondary flow.

The analytical model provides information about the flow regime inside the supersonic geoejector; nevertheless, a numerical model is required to identify the underlying transport phenomena for heat, momentum, and mass transfer. Figure 5.18 shows the pressure, Mach No., and enthalpy profile produced from the numerical model at the operating conditions provided by the field operators (Numerical model inputs: p_{1-0}=25.03 bar-g, p_{5-0}=9 bar-g, T_{1-0}=226.16 °C, T_{4-0}=176.9 °C, x_1=1, x_5 =0.093, and p_9=10.48 bar-g).

(a)

(b)

(c)
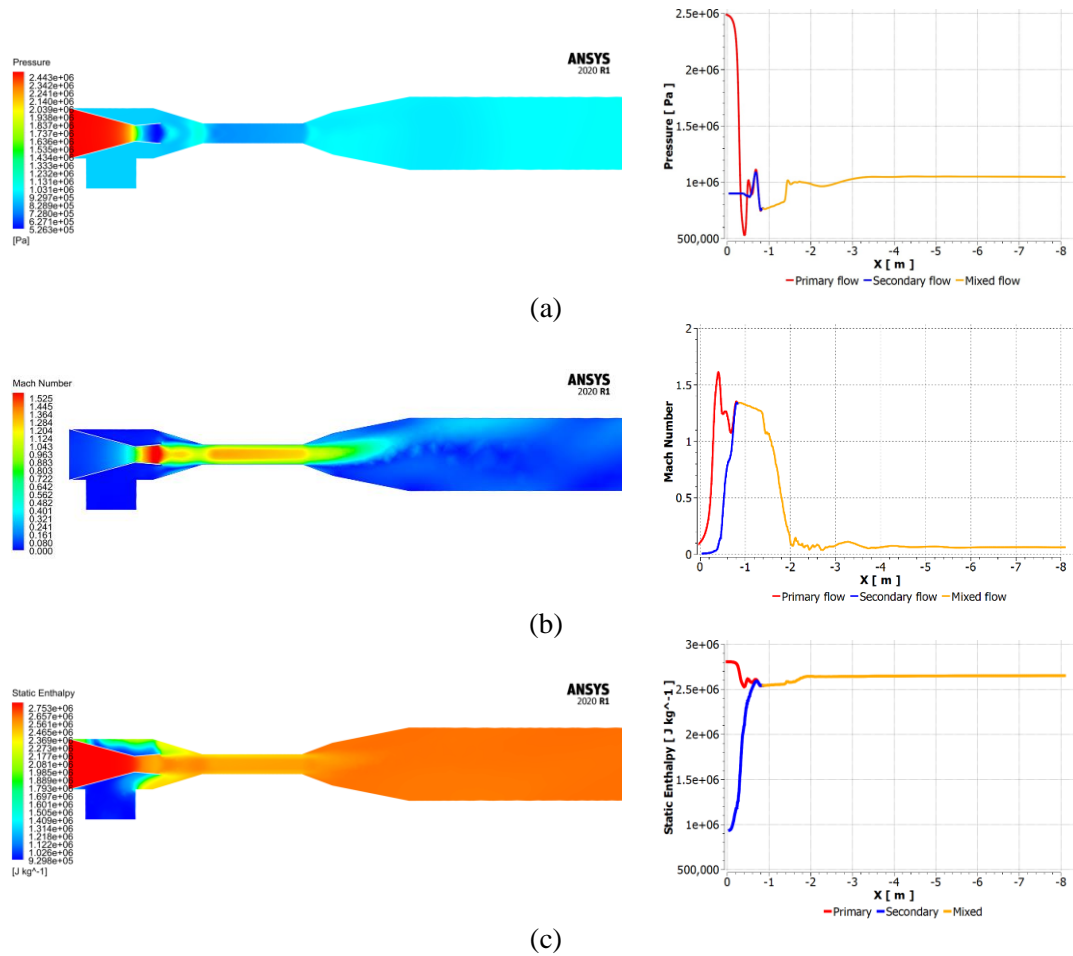
Figure 5.18 (a) Pressure, (b) Mach Number, and (c) enthalpy profile of supersonic geoejector.

From Figure 5.18, the nozzle accelerates the primary fluid to supersonic speed at Mach 1.55 and reduces its pressure to 5.63 bar-g. A shockwave occurs when the primary fluid exited the nozzle, resulting in a decrease in flow speed (Mach No. 1.08) and an increase in pressure (11.08 bar-g). As the primary flow chokes at the hypothetical throat, the primary fluid was accelerated up to Mach No. 1.35, resulting in a 7.68 bar-g underpressure that induces flow from the secondary inlet. The induced flow was also choked at the hypothetical throat, causing the stream to accelerate to Mach No. 1. At the hypothetical throat, both the primary and secondary streams mixed with pressures and Mach No. of 7.68 bar-g and 1.34, respectively. The mixed flow is subsequently decelerated at the constant area mixing section by a shockwave, which raises the pressure of the mixed flow to 9.85 bar-g. The flow is then decelerated further in a diffuser to achieve pressure and enthalpy values of 10.48 bar-g and 2652.77 kJ/kg, respectively. The analytical model yielded mass flows of 28.22 and 3.00 kg/s for the primary and secondary inlets, respectively.

The supersonic geoejector results were limited to analytical and numerical models. The output of the supersonic geoejector could not be validated in the absence of field test data or experiments. Despite this, the performance of the supersonic geoejector was predicted and compared in different pressures at the primary and secondary inlet, as shown in Figure 5.19, using the operating parameters indicated in Figure 5.11. The figure shows that only the mass flow from the primary inlet exhibits good agreement between the two models, with a relative difference ranging from 3.57 to 4.09%. The mass flow for the secondary inlet, on the other

hand, varies significantly from 66.99 to 76.61%. The variation in the secondary inlet was carried over to the enthalpy at the outlet, which had a relative difference ranging from 11.63 to 17.27%.
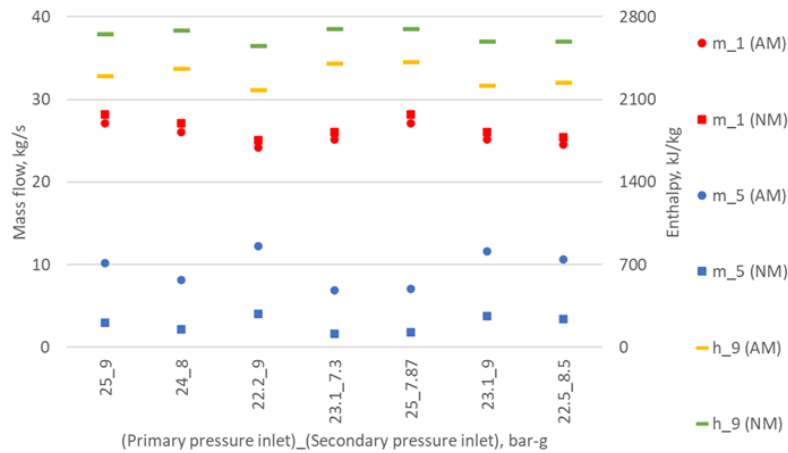
Figure 5.19 Comparison of analytical (AM) and numerical model (NM).

The pressure, Mach No., and enthalpy profile of the models were plotted together to identify the difference between the analytical and numerical model results (see Figure 5.20). According to the figure, one of the biggest discrepancies within the profiles is the shockwave that occurs at the primary flow leaving the nozzle (location 3) in the numerical model. The pressure of the primary fluid before the hypothetical throat (location 4&6) increased as a result. Despite this, as the streams accelerated in the mixing chamber (location 3.5) before the hypothetical throat, underpressure was formed allowing entrainment to the secondary flow.
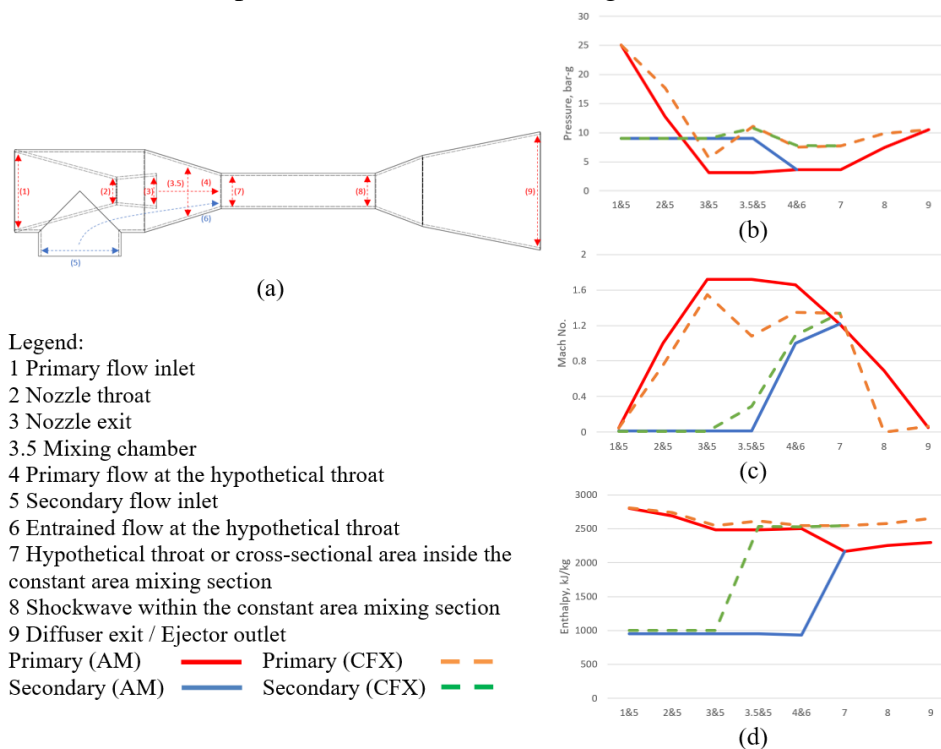
Figure 5.20 Predicted flow regime for the supersonic geoejector from the analytical.

Notwithstanding the differences in the analytical and numerical model results, the generated profiles in Figure 5.20 show similarities in the flow regime determined both models. In order to better understand the source of their difference, two factors were explored to

determine their impact on the outcomes (see Figure 5.21). On the figure, the steam quality values at the secondary inlet were varied to test the models' sensitivity (from the approximated steam quality at the operating condition of 0.093 to 1). Second, to examine the sensitivity of the analytical model, the losses inside the model were ignored (c_l and η_n are equal to 1 instead of 0.84 and 0.9, respectively).
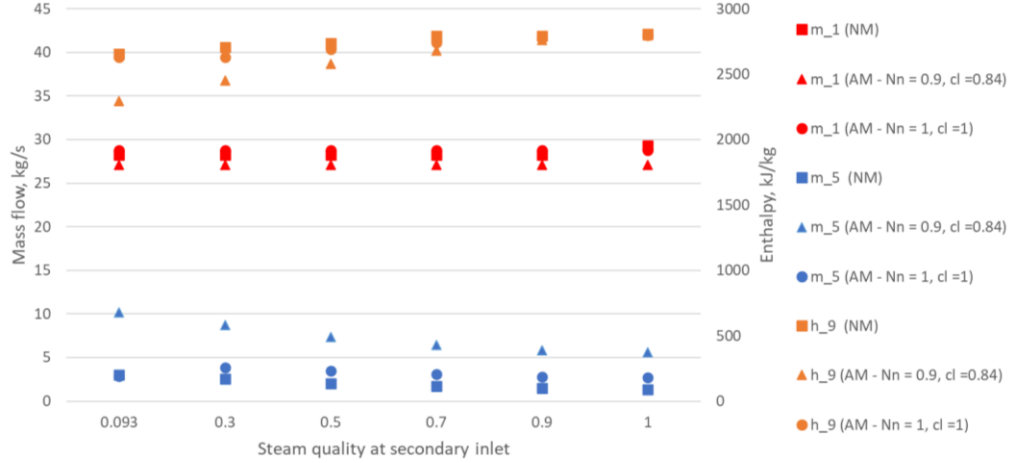
Figure 5.21 Analysis on the relative difference of results between the analytical and numerical model.

Figure 5.21 shows that when the steam quality of the secondary inlet was increased to 1 in both the analytical (with losses, c_l=0.84 and η_n=0.9) and numerical models, the relative difference in enthalpy at the outlet decreases from 15.51 to 0.31%. However, the relative difference at the secondary mass flow inlet has increased from 70.53 to 75.37%. On the other hand, when the losses in the analytical model were disregarded (c_l and η_n are equal to 1), the analytical and numerical models improved their agreement. When the steam quality at the secondary flow is 0.093, the relative difference between the analytical (without losses) and numerical model for the secondary mass flow inlet decreases from 70.53 to 3.18%. Better agreement was also seen in terms of relative difference in primary mass flow input (from 4.09% to 1.90%) and enthalpy at outflow (from 15.51% to 0.80%). Yet, should the steam quality of the secondary flow at the inlet increased, the relative difference in the entrained flow increased up to 49.26%, while the primary inlet pressure and enthalpy at the exit remained in good agreement.

The results demonstrate that the losses in the streams were one of the factors contributing to the relative difference between the analytical and numerical models. Due to the absence of losses, the primary stream occupies more area within the hypothetical throat, reducing entrained flow (see Equation 11 at Appendix B). However, it is believed that there are still underlying factors, such as geometric parameters, may have influenced the difference between the analytical and numerical model results.

Chapter 6

Conclusion and recommendations

This study is intended to be as a preliminary step toward the development of a geoejector, which could be utilized to extract energy from a low-pressure and low-enthalpy well. This study examined the field test conducted at the Theistareykir Geoethermal Field and developed both an analytical and a numerical model to analyze its performance. The results of this investigation were then used to develop a new design of the geoejector that meets the requirements of the geothermal field. The main findings of the study can be summarized as:

1. Field test results shows that the subsonic geoejector entrained flow from the secondary stream and subsequently resulted in an increase in pressure at the outlet as it mixes to the primary stream. However, changes in useful energy should be taken into account to ensure that the use of geoejectors is beneficial for power generation.

2. The field test measurements of the subsonic geoejector demonstrate better agreement with the analytical model results (with a maximum relative error of 13.01% at the outlet pressure) than the numerical model (with a maximum relative error of 23.80% at the primary inlet pressure).

3. The analytical and numerical models for the subsonic geoejector revealed that the nozzle was insufficient to provide an underpressure to properly entrain the secondary flow. Consequently, operating THG-11 at its normal operating conditions (i.e. for a primary inlet pressure of 25 bar-g, the nozzle exit pressure is estimated to be 17.57 bar-g) may result in backflow to the secondary inlet due to a considerable pressure difference inside the mixing chamber.

4. The shear stress caused by difference of speed between the primary and secondary streams leads to an increase in losses in the system. To ensure that minimal losses occur within the systems, the secondary flow should be choked at the mixing section to induce sonic flow.

5. The supersonic geoejector was designed based on the realistic operating conditions in the field. According to the model, a minimum pressure from the secondary inlet is necessary to keep the back pressure and pressure inside the mixing chamber within the defined constraints. Furthermore, the operational range in Figure 5.11 indicate that the primary and secondary well pressures could go as low as 22.2 bar-g and 7.2 bar-g, respectively.

6. Significant relative difference from 66.99 to 76.61% were found in the predicted secondary mass flow between the analytical and numerical model for the supersonic geoejector. This huge difference could be attributed to the losses added in the analytical model as well as other underlying factors such as geometric parameters.

7. Subsonic and supersonic geoejector has an energy conversion efficiency, $\eta_{\Delta \dot{H}}$, of 20.42% and 25.67%, respectively. Due to the difference of input in both models, the $\eta_{\Delta \dot{H}}$ could not be directly compared.

8. Based on the operational range in Figure 5.11, the analytical model suggests that using a supersonic geoejector might result in an additional potential for power generation of around 0.5 to 0.8 MWe, or 25% to 40% of the wellhead potential of well THG-15.

9. Field test of the supersonic geoejector is required to collect more information about flow conditions (such as local pressures, velocity profiles, turbulence intensity, and steam quality) in order to improve both the analytical and numerical models.

10. Further study on the shear stress would improve the accuracy of the analytical model in predicting the performance of the geoejector.

11. The analytical model could not predict the impact of changing various geometric parameters (i.e. NXP and constant area mixing section length). To better understand their influence, controlled experiments are required.

12. The existence of a high-pressure well and low-pressure well within a geothermal field is not unique in Theistareykir Geothermal Field. Similar cases could be found in the Philippines and probably other countries with high-temperature geothermal fields. Doing similar study in different geothermal field would be valuable in order to better understand the factors that influence the geoejector's performance.

13. The geoejector could be an effective alternative to handle the silica scaling problem at THG-11 because when liquid from THG-15 is mixed with the stream of THG-11, power from THG-15 can be recovered for additional power generation.

14. Further research into modifying the geoejector into a multi-stage geoejector could broaden the system's application into various geothermal fields that has no high-pressure wells similar to THG-11.

Bibliography

Ameur, K., Aidoun, Z., & Ouzzane, M. (2016). Modeling and numerical approach for the design and operation of two-phase ejectors. *Applied Thermal Engineering*, *109*, 809–818. https://doi.org/10.1016/j.applthermaleng.2014.11.022

ANSYS Inc. (2023a). *ANSYS CFX-introduction*. Canonsburg, PA.

ANSYS Inc. (2023b). *ANSYS CFX-solver modeling guide* . Canonsburg, PA.

ANSYS Inc. (2023c). *ANSYS CFX-solver theory guide.* Canonsburg, PA.

ANSYS Inc. (2023d). *ANSYS Fluent user's guide*. Canonsburg, PA.

Aphornratana, S., Chungpaibulpatana S., & Srikhirin, P. (2001). Experimental investigation of an ejector refrigerator: Effect of mixing chamber geometry on system performance. I*nternational Journal of Energy Research*, *25*. 397 - 411.

Bartosiewicz, Y., Aidoun, Z., Desevaux, P., & Mercadier, Y. (2005). Numerical and experimental investigations on supersonic ejectors. *International Journal of Heat and Fluid Flow*, *26(1)*, 56–70. https://doi.org/10.1016/j.ijheatfluidflow.2004.07.003

Besagni, G. (2019). Ejectors on the cutting edge: The past, the present and the perspective. *Energy*, *170*, 998–1003. https://doi.org/10.1016/j.energy.2018.12.214

Bejan, A., Moran, M., and Tsatsaronis, G., (1996). *Thermal design and optimization*. John Wiley & Sons, Inc., Canada, 533 pp.

Bell, I. H., Wronski, J., Quoilin, S., & Lemort, V. (2014). Pure and Pseudo-pure Fluid Thermophysical Property Evaluation and the Open-Source Thermophysical Property Library CoolProp. *Industrial & Engineering Chemistry Research*, *53(6)*. 2498–2508. https://doi.org/10.1021/ie4033999

Chen, W., Chong, D., Yan, J., & Liu, J. (2013). The numerical analysis of the effect of geometrical factors on natural gas ejector performance. *Applied Thermal Engineering*, *59(1–2)*, 21–29. https://doi.org/10.1016/j.applthermaleng.2013.04.036

Chen, W., Shi, C., Zhang, S., Chen, H., Chong, D., & Yan, J. (2017). Theoretical analysis of ejector refrigeration system performance under overall modes. *Applied Energy*, *185*, 2074–2084. https://doi.org/10.1016/j.apenergy.2016.01.103

Clark, C. E., Harto, C. B., Sullivan, J. L., & Wang, M. Q. (2011). *Water use in the development and operation of geothermal power plants*. In: ANL/EVS/R-10/5. U.S. Department of Energy, Office of Energy Efficiency and Renewable Energy (EERE), Geothermal Technologies Program. Argonne, IL: Argonne National Laboratory.

Climate-Data.org. (2023). *Húsavík* climate. Retrieved March 16, 2023, from https://en.climate-data.org/europe/iceland/husavik/husavik-24810/#climate-table

Colarossi, M., Trask, N., Schmidt, D. P., & Bergander, M. J. (2012). Multidimensional modeling of condensing two-phase ejector flow. *International Journal of Refrigeration*, *35(2)*, 290–299. https://doi.org/10.1016/j.ijrefrig.2011.08.013

DOE (2023). *Geothermal well inventory in the Philippines*. Department of Energy, Taguig, Philippines, unpublished internal report

Dincer, I. & Rosen, M. A. (2020). *Exergy: Energy, environment and sustainable development* (3rd ed.). Elsevier.

Ding, Z., Wang, L., Zhao, H., Zhang, H., & Wang, C. (2016). Numerical study and design of a two-stage ejector for subzero refrigeration. *Applied Thermal Engineering*, *108*, 436–448. https://doi.org/10.1016/j.applthermaleng.2016.07.104

Djajadiwinata, E., Sadek, S., Alaqel, S., Orfi, J., & Al-Ansary, H. (2021). Numerical and One-Dimensional Studies of Supersonic Ejectors for Refrigeration Application: The Significance of Wall Pressure Variation in the Converging Mixing Section. *Applied Sciences*, *11(7)*, 3245. https://doi.org/10.3390/app11073245

Egilson, T., (2019). *Þeistareykir Eftirlitsmælingar árið 2018*, Iceland GeoSurvey report ISOR-2019/029, 41 pp.

Gehringer, M. & Loksha, V.C. (2012). *Geothermal Handbook: Planning and Financing Power*

Generation. Washington DC: World Bank Group, Energy Sector.

Gutsol, A. F. (2018). Ejector for Geothermal Well Lifetime Increase, *GRC Transaction*, *Vol. 42*, 6.

Huang, B. J., Chang, J. M., Wang, C. P., & Petrenko, V. A. (1999). A 1-D analysis of ejector performance. *International Journal of Refrigeration*, *22(5)*, 354–364. https://doi.org/10.1016/S0140-7007(99)00004-3

IFC (2013). *Success of geothermal wells: a global study. International Finance Corporation*, World Bank Group, Washington, DC, 76 pp.

Jung, D. B. (1999). *Eductor/ejector apparatus and the process for increasing fluid recovery from geothermal wells*. US Patent 5899273A.

Keenan, J. H. & Neumann, E. P. (1942). A simple air ejector. *Journal of Applied Mechanics*, *Trans. ASME 64*, 75-81.

Keenan, J. H. and Neumann, E. P., & Lustwerk, F. (1950). An investigation of ejector design by analysis and experiment. *Journal of Applied Mechanics*, *Trans. ASME 17*, 299-309.

Knútsson, V., Geirsson, S. B., Hjartarson, H., & Emilsson, J. A. (2018). Theistareykir Geothermal Power Plant, A Sustainable Construction. *GRC Transaction*, *Vol. 42*.

Mkangala, A. (2017). Borehole geology of Well THG-15 at Theistareykir Geothermal Field, NE-Iceland. *Report 18 in: Geothermal Training in Iceland, UNU-GTP in Iceland*, 297-316.

Munday, J. T. & Bagster, D. F. (1977). A new ejector theory applied to steam jet refrigeration. *Ind. Eng. Chem. Process. Des. Dev. 16*, *(4)*, 442-449.

Pianthong, K., Seehanam, W., Behnia, M., Sriveerakul, T., & Aphornratana, S. (2007). Investigation and improvement of ejector refrigeration system using computational fluid dynamics technique. *Energy Conversion and Management*, *48(9)*, 2556–2564. https://doi.org/10.1016/j.enconman.2007.03.021

Ringstad, K. E., Allouche, Y., Gullo, P., Ervik, Å., Banasiak, K., & Hafner, A. (2020). A detailed review on CO 2 two-phase ejector flow modeling. *Thermal Science and Engineering Progress*, *20*, 100647. https://doi.org/10.1016/j.tsep.2020.100647

Šarevski, V. V. & Šarevski, M. (2019). Flow characteristics, modeling and simulation of single-phase and two-phase ejectors. *Zbornik Međunarodnog kongresa o KGH*, *45(1)*, 1-11.

Sriveerakul, T., Aphornratana, S., & Chunnanond, K. (2007). Performance prediction of steam ejector using computational fluid dynamics: Part 1. Validation of the CFD results. International *Journal of Thermal Sciences*, *46(8)*, 812–822. https://doi.org/10.1016/j.ijthermalsci.2006.10.014

Wagner, W., & Pruss, A., (2002). The IAPWS Formulation 1995 for the Thermodynamic Properties of Ordinary Water Substance for General and Scientific Use. *Journal of Physical and Chemical Reference Data*, *31(2)*, 387–535. https://doi.org/10.1063/1.1461829

Wagner, W., and Kruse, A. (1998), "*The Industrial Standard IAPWS-IF97: Properties of Water and Steam*", Springer, Berlin.

White, F. (2011). *Fluid mechanics, eighth edition*. New York: McGraw-Hill Education.

Zhu, Y., & Jiang, P. (2014). Experimental and numerical investigation of the effect of shock wave characteristics on the ejector performance. *International Journal of Refrigeration*, *40*, 31–42. https://doi.org/10.1016/j.ijrefrig.2013.11.008

Appendix A Governing equations for subsonic geoejector

This part of the study provides information on the governing equations found in the analytical model for the subsonic geoejector, see Figure A.1. Subscript numbers in the figure refer to locations in Figure A.2.
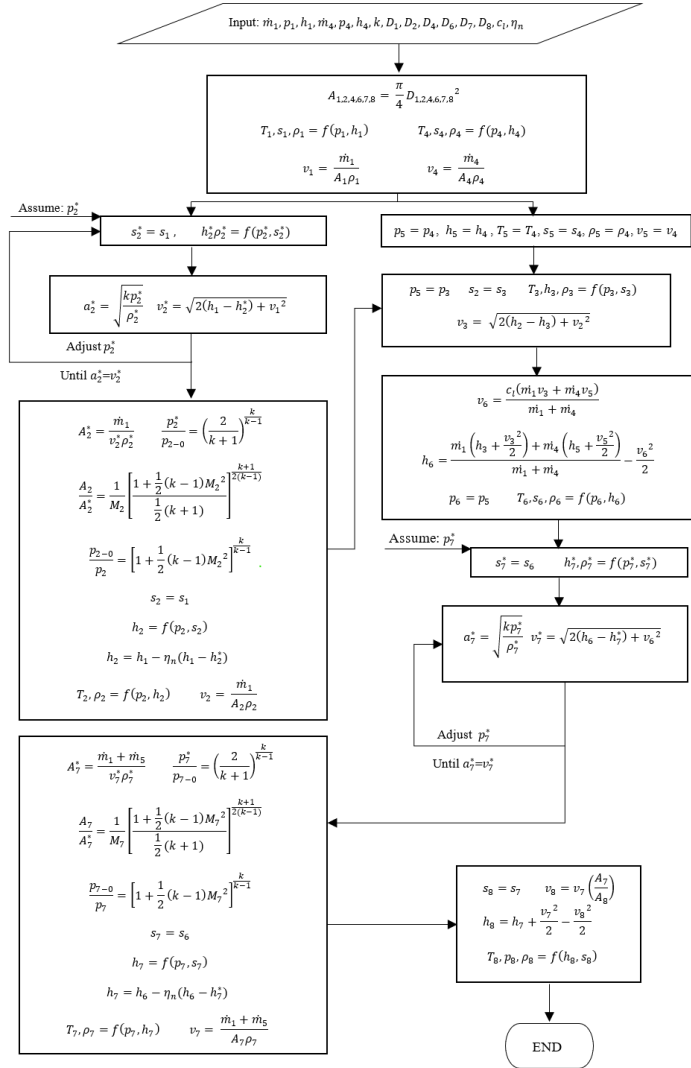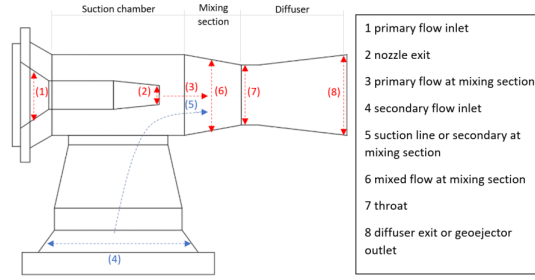

Figure A.1 Flowchart of the analytical model of the subsonic geoejector.

1	primary flow inlet
2	nozzle exit
3	primary flow at mixing section
4	secondary flow inlet
5	suction line or secondary at mixing section
6	mixed flow at mixing section
7	throat
8	diffuser exit or geoejector outlet

Figure A.2 Subsonic geoejector used during field test at Theistareykir Geothermal Field.

Nozzle (2): the acceleration of the primary fluid follows the gas dynamic relations between the Mach No. at the exit of nozzle (M_2) and the cross-section area (A_2) as shown in Equation 1.

$$\frac{A_2}{A_2^*} = \frac{1}{M_2}\left[\frac{1 + \frac{1}{2}(k-1){M_2}^2}{\frac{1}{2}(k+1)}\right]^{\frac{k+1}{2(k-1)}}$$

(6.1)

The pressure at the nozzle exit, p_2, can be calculated using isentropic relation shown in Equation 2.

$$\frac{p_{2-0}}{p_2} = \left[1 + \frac{1}{2}(k-1){M_2}^2\right]^{\frac{k}{k-1}}$$

(6.2)

Given the isentropic efficiency, η_n , of the compressible flow in the nozzle and the isentropic enthalpy h_2^* obtained from the calculated pressure and entropy, h_2 can be adjusted using Equation 3.

$$h_2 = h_1 - \eta_n(h_1 - h_2^*)$$

(3)

Suction line or secondary flow at the mixing section (5): it is assumed that the properties of the secondary flow are constant from the inlet up to the suction line, as shown in Equation 4.

$$p_5 = p_4 \, , h_5 = h_4 \, ; T_5 = T_4 \, , s_5 = s_4 \, , \rho_5 = \rho_4 \, , v_5 = v_4$$

(4)

Primary flow at the mixing section (3): it is further assumed that the entropy of the primary flow remains constant from the outlet of the nozzle (2) to the suction line (3) and that the primary and secondary streams start to mix with uniform pressure, equal to the pressure of the secondary flow at the mixing section (5), as shown in Equation 5.

$$s_3 = s_2 \quad p_3 = p_5$$

(5)

Mixing flow at mixing section (6): in this section of the geoejector, it is assumed that the primary and secondary flow will mix at a constant pressure equal to the pressure of the secondary flow at the suction line ($p_5 = p_6$). The properties in the mixing chamber can be

calculated using the conservation of momentum and energy, as shown in Equation 6 and 7, respectively.

$$v_6 = \frac{c_l(\dot{m}_1 v_3 + \dot{m}_4 v_5)}{\dot{m}_1 + \dot{m}_4}$$

(6)

$$h_6 = \frac{\dot{m}_1\left(h_3 + \frac{v_3^2}{2}\right) + \dot{m}_4\left(h_5 + \frac{v_5^2}{2}\right)}{\dot{m}_1 + \dot{m}_4} - \frac{v_6^2}{2}$$

(7)

Mixing section's throat (7): as with the flow inside the primary nozzle, the flow in the mixing chamber is assumed to be isentropic. Thus Equations 8 and 9 are used to calculate the fluid properties.

$$\frac{A_7}{A_7^*} = \frac{1}{M_7}\left[\frac{1 + \frac{1}{2}(k-1)M_7^2}{\frac{1}{2}(k+1)}\right]^{\frac{k+1}{2(k-1)}}$$

(8)

$$\frac{p_{7-0}}{p_7} = \left[1 + \frac{1}{2}(k-1)M_7^2\right]^{\frac{k}{k-1}}$$

(9)

Given the isentropic efficiency η_n, and the isentropic enthalpy h_7^*, obtained from the calculated pressure and entropy, h_7 can be adjusted using Equation 10.

$$h_7 = h_6 - \eta_n(h_6 - h_7^*)$$

(10)

Diffuser (8): the diffuser decelerates the fluid to recover the pressure. To calculate the properties at the diffuser's outlet, the steady one-dimensional incompressible continuity equation, as shown in Equation 11, is used.

$$v_8 = v_7\left(\frac{A_7}{A_8}\right)$$

(11)

The enthalpy at the diffuser's outlet (h_8) can be obtained through energy balance, as shown in Equation 12, while the rest of the properties at the diffuser outlet are obtained by assuming that the entropy at the mixing chamber's throat is equal to the entropy at the diffuser outlet.

$$h_8 = h_7 + \frac{v_7^2}{2} - \frac{v_8^2}{2}$$

(12)

Appendix B Governing equations for supersonic geoejector

This part of the study provides information on the governing equations found in the analytical model for the supersonic geoejector, see Figure B.1. Subscript numbers in the figure refer to locations in Figure B.2.
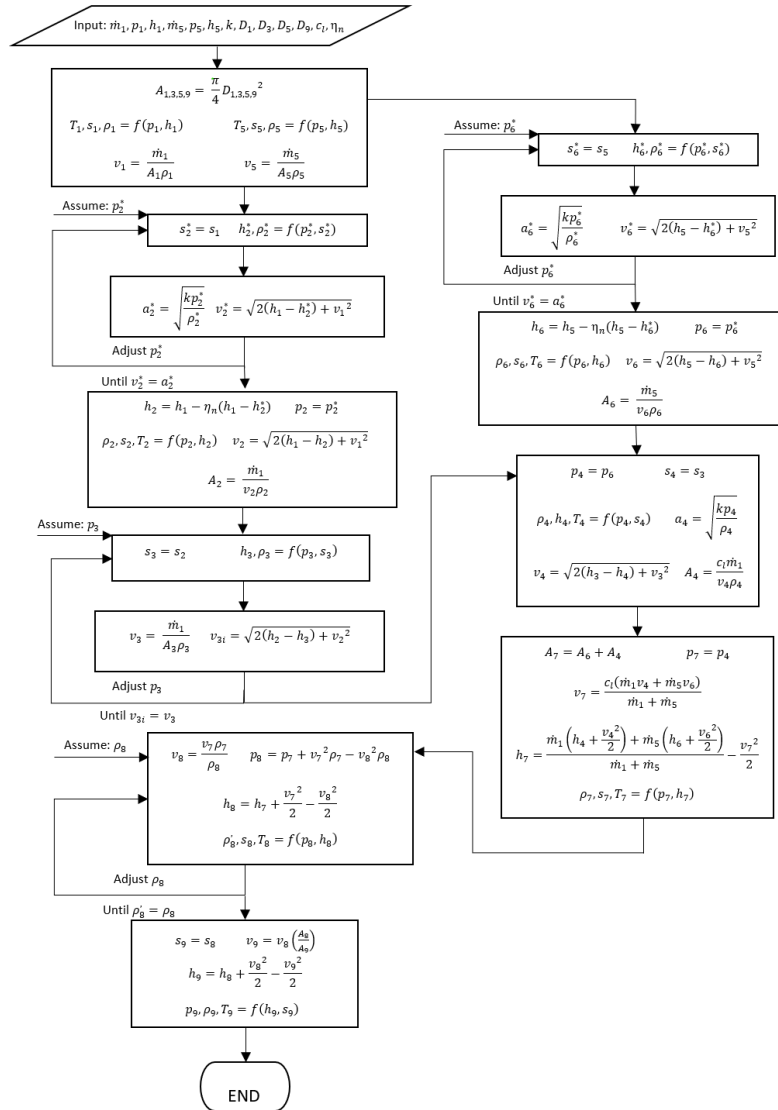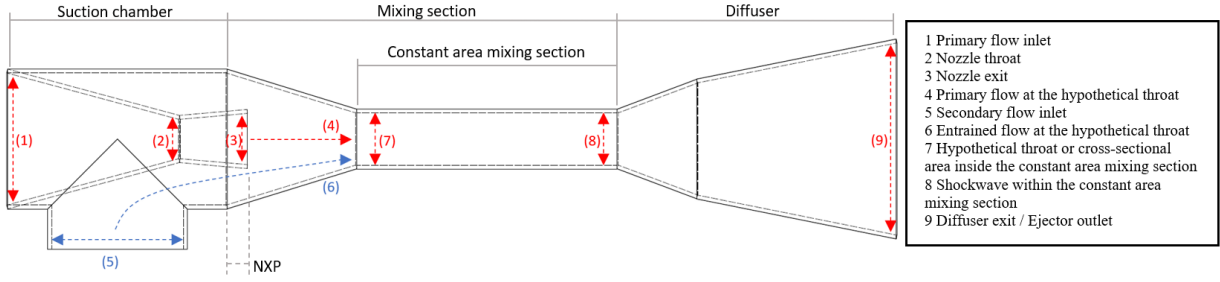

Figure B.1 Flowchart of the analytical model of the supersonic geoejector.

Figure B.2 Supersonic geoejector designed for Theistareykir Geothermal Field.

Nozzle throat (2): to get a supersonic flow from the nozzle, the throat should accelerate the primary fluid until it reaches sonic flow. With this, the pressure, p_2, and the enthalpy, h_2, at the throat, can be determined by iterating p_2 until the fluid velocity, v_2^*, becomes critical, i.e. equal to sonic velocity, a_2^*, as shown in Equation 1 and 2, respectively (subscript numbers refer to locations in Figure 3.4).

$$v_{2|p2}^* = \sqrt{2\left(h_1 - h_{2|p_2}^*\right) + v_1{}^2} \tag{1}$$

$$a_{2|p2}^* = \sqrt{\frac{kp_2}{\rho_{2|p_2}^*}} \tag{2}$$

Considering the isentropic efficiency, η_n, of the compressible flow in the nozzle, the enthalpy obtained from the isentropic enthalpy, h_2^*, can be adjusted using Equation 3.

$$h_2 = h_1 - \eta_n(h_1 - h_2^*) \tag{3}$$

With the calculated pressure, p_2, obtained from Equations 1 and 2, and adjusted enthalpy, h_2, from Equation 3, the velocity and density at the throat can then be determined. These values, along with the mass flow rate, $\dot{m}_1$, are needed to get the area at the throat, A_2, as shown in Equation 4.

$$A_2 = \frac{\dot{m}_1}{v_2 \rho_2} \tag{4}$$

Nozzle exit (3): in this section of the model, it is important to assign a temporary value for the diameter of the nozzle exit, D_3. This can later be optimized to make sure that all the constraints are met. After assigning a value, the pressure at the nozzle exit, p_3, will be iterated until the two formulas for velocity, as shown in Equations 5 and 6, give equal results.

$$v_3 = \frac{\dot{m}_1}{\rho_{3|p_3} A_3} \tag{5}$$

$$v_3' = \sqrt{2\left(h_2 - h_{3|p_3}\right) + v_2{}^2} \tag{6}$$

Entrained flow at the hypothetical throat (6): the entrained secondary flow is assumed to reach sonic, or choking condition, at the hypothetical throat. To calculate the pressure, p_6, and enthalpy, h_6, of the secondary flow in this area, the value of the pressure should be iterated until the fluid velocity, v_6^*, becomes critical, i.e. equal to sonic velocity, a_6^*, as shown in Equation 7 and 8, respectively.

$$v_{6|p6}^* = \sqrt{2\left(h_5 - h_{6|p_6}^*\right) + v_5{}^2}$$

(7)

$$a_{6|p_6}^* = \sqrt{\frac{kp_6}{\rho_{6|p_6}^*}}$$

(8)

Considering the isentropic efficiency, η_n, the enthalpy obtained from the isentropic enthalpy, h_6^* can be adjusted using Equation 9.

$$h_6 = h_5 - \eta_n(h_5 - h_6^*)$$

(9)

With the calculated pressure, p_6, from Equation 7 and 8, and adjusted enthalpy, h_6, from Equation 9, the velocity and density of the secondary flow before the hypothetical throat can then be calculated. These values, along with the mass flow rate, $\dot{m}_5$, are needed to get the area of the hypothetical throat occupied by the entrained flow, A_6, as shown in Equation 10.

$$A_6 = \frac{\dot{m}_5}{v_6 \rho_6}$$

(10)

Primary flow at the hypothetical throat (4): it was assumed that the two streams start to mix with uniform pressure equal to the pressure of the entrained flow at the hypothetical throat, p_6. Additionally, it was assumed that the flow from the nozzle exit to the hypothetical throat is isentropic. In contrast, a loss coefficient, c_l, is included in calculating the area of the hypothetical throat occupied by the primary flow, A_4, as shown in Equation 11.

$$A_4 = \frac{c_l \dot{m}_1}{v_4 \rho_4}$$

(11)

Hypothetical throat or cross-sectional area inside the constant area mixing section (7): the sum of the areas of the primary and entrained flow before the hypothetical throat will then be equal to the area of the constant area mixing section, as shown in Equation 12.

$$A_7 = A_6 + A_4$$

(12)

It was further assumed that the two streams would start to mix inside the constant area mixing section. A momentum balance relationship with the inclusion of losses can be used to determine the velocity, v_7, as shown in Equation 13.

$$v_7 = \frac{c_l(\dot{m}_1 v_4 + \dot{m}_5 v_6)}{\dot{m}_1 + \dot{m}_5}$$

(13)

Additionally, the enthalpy, h_7, can be determined using the energy balance relation as shown in Equation 14.

$$h_7 = \frac{\dot{m}_1\left(h_4 + \frac{v_4{}^2}{2}\right) + \dot{m}_5\left(h_6 + \frac{v_6{}^2}{2}\right)}{\dot{m}_1 + \dot{m}_5} - \frac{v_7{}^2}{2}$$

(14)

Shock wave within the constant area mixing section (8): The flow is compressed and decelerated to subsonic velocities through a shockwave. To determine the flow property changes in this section, the density, ρ_8, will be iterated until it satisfies the conditions for the continuity, momentum, and energy equation, as shown in Equations 15-17. The pressure and enthalpy obtained will then be used to determine the remaining properties in this section, see Equation 18. The iteration will continue until $\rho_8 = \rho'_8$.

$$v_{8|\rho_8} = \frac{v_7 \rho_7}{\rho_8}$$

(15)

$$p_{8|\rho_8} = p_7 + v_7{}^2 \rho_7 - v_{8|\rho_8}{}^2 \rho_8$$

(16)

$$h_{8|\rho_8} = h_7 + \frac{v_7{}^2}{2} - \frac{v_{8|\rho_8}{}^2}{2}$$

(17)

$$\rho'_{8|\rho_8}, \; s_{8|\rho_8}, \; T_{8|\rho_8} = f\left(p_{8|\rho_8}, h_{8|\rho_8}\right)$$

(18)

Diffuser exit or Geoejector exit (9): the diffuser will further decelerate the fluid and increase the pressure. To obtain the properties at the diffuser exit, the steady one-dimensional incompressible continuity equation, as shown in Equation 19, is used to calculate the velocity, v_9, after the diffuser.

$$v_9 = v_8 \left(\frac{A_8}{A_9}\right)$$

(19)

After obtaining the velocity, the enthalpy, h_9, at the diffuser exit could be obtained through the energy balance equation, as shown in Equation 20. While the rest of the properties at the diffuser exit could be obtained by assuming that the entropy after the shock, s_8, is equal to the entropy at the diffuser exit, s_9.

$$h_9 = h_8 + \frac{v_8{}^2}{2} - \frac{v_9{}^2}{2}$$

(1)

Appendix C Grid convergence studies

To assess the variance of the computed solution and reduce the computational time, a grid convergence study was performed in three grid levels (coarse, fine, and very fine) for both subsonic (Table C.1) and supersonic geoejectors (Table C.2). The computed solution on the measurement points set on the model (a. Subsonic geoejector: static pressure at the primary and secondary inlet, and enthalpy at the outlet; b. Supersonic geoejector: mass flow rate at the primary and secondary inlet and enthalpy at the outlet) for the coarse and fine mesh will be compared to the computed solution for the very fine mesh.

Table 1 shows that the variations in the computed solutions among the grids are minimal, with 0.03 to 0.48% relative difference across the measurement points. This result is not surprising as the configuration of the boundary conditions used for the subsonic geoejector is the most robust for ANSYS CFX. Using the coarse grid for the numerical modelling of the subsonic geoejector will provide a minimize the discretization error in the numerical simulations and decrease in computational cost of about 63.77%.

Table C.1 Grid convergence study - subsonic geoejector.

Description	Coarse	Fine	Very fine
Nodes	51 449	88 213	135 416
Elements	135 686	246 326	387 444
Primary pressure, bar-g	11.1643	11.1628	11.1678
(Percentage difference, %)	(0.03%)	(0.04%)	(0.00%)
Secondary pressure, bar-g	10.7948	10.7944	10.7952
(Percentage difference, %)	(0.00%)	(0.01%)	(0.00%)
Outlet enthalpy, kg/s	1624.24	1622.85	1630.66
(Percentage difference, %)	(0.39%)	(0.48%)	(0.00%)
Time per iteration, sec/iteration	3.88	6.04	10.71

Table 2 shows that the variations in the computed solutions between fine and very fine grid is minimal, with a maximum relative difference of 1.42% across the measurement points. On the other hand, the coarse and very fine grid has a significant difference in the computed solution for suction flow with 18.93%. Using the fine grid for the numerical modelling of the subsonic geoejector will provide a minimize the discretization error in the numerical simulations and decrease in computational cost of about 46.81%.

Table C.2 Grid convergence study - supersonic geoejector.

Description	Coarse	Fine	Very fine
Nodes	55 914	96 023	117 988
Elements	147 335	245 199	336 793
Primary flow, kg/s	28.203	28.217	28.261
(Percentage difference, %)	(0.20%)	(0.16%)	(0.00%)
Suction flow, kg/s	2.394	2.995	2.953
(Percentage difference, %)	(18.93%)	(1.42%)	(0.00%)
Outlet, kg/s	30.521	31.399	31.223
(Percentage difference, %)	(2.25%)	(0.56%)	(0.00%)
Time per iteration, sec/iteration	3.48	4.84	9.10

Tækni- og verkfræðideild
Háskólinn í Reykjavík
Menntavegi 1
101 Reykjavík, Ísland
Sími +354 599 6200
Fax +354 599 6201
www.ru.is